AD-A175 093

RESEARCH AND DEVELOPMENT TECHNICAL REPORT
CECOM-TR-82-J069-F

IN-BAND ANTENNA COUPLING RESEARCH

B.J. Cown, C.D. Papanicolopolus, and R.W. Cravey

Georgia Institute of Technology
Georgia Tech Research Institute
Electronics and Computer Systems Laboratory
Atlanta, GA 30332

June 1986

Final Report for Period March 1982 - December 1984

DTIC
ELECTE
DEC 1 5 1986
S   D
B

Prepared for

Communications/Automated Data Processing Center

CECOM

U S ARMY COMMUNICATIONS-ELECTRONICS COMMAND
FORT MONMOUTH, NEW JERSEY 07703

86 12 15 017

REPORT DOCUMENTATION PAGE

1a. REPORT SECURITY CLASSIFICATION	1b RESTRICTIVE MARKINGS
Unclassified	

2a. SECURITY CLASSIFICATION AUTHORITY	3 DISTRIBUTION/AVAILABILITY OF REPORT
	Approved for public release; distribution
2b. DECLASSIFICATION/DOWNGRADING SCHEDULE	is unlimited.

4. PERFORMING ORGANIZATION REPORT NUMBER(S)	5. MONITORING ORGANIZATION REPORT NUMBER(S)
A-3213	CECOM-TR-82-J069-F

6a. NAME OF PERFORMING ORGANIZATION	6b. OFFICE SYMBOL (If applicable)	7a. NAME OF MONITORING ORGANIZATION
Georgia Institute of Technology Engineering Experiment Station		US Army Communications-Electronics Cmd (CECOM Communications/Automated Data Processing Ctr

6c. ADDRESS (City, State, and ZIP Code)	7b. ADDRESS (City, State, and ZIP Code)
Electronics and Computer Systems Laboratory Electromagnetic Effectiveness Division Atlanta, GA 30332	USA CECOM, Comm/ADP Center ATTN: AMSEL-COM-AY-2 Fort Monmouth, NJ 07703-5202

8a. NAME OF FUNDING/SPONSORING ORGANIZATION	8b. OFFICE SYMBOL (If applicable)	9. PROCUREMENT INSTRUMENT IDENTIFICATION NUMBER
		DAAB07-82-C-J069

8c. ADDRESS (City, State, and ZIP Code)	10 SOURCE OF FUNDING NUMBERS			
	PROGRAM ELEMENT NO.	PROJECT NO.	TASK NO.	WORK UNIT ACCESSION NO.

11. TITLE (Include Security Classification)

IN-BAND ANTENNA COUPLING RESEARCH (U)

12. PERSONAL AUTHOR(S) B.J. Cown, C.D. Papanicolopolus, and R.W. Cravey

13a. TYPE OF REPORT	13b. TIME COVERED	14. DATE OF REPORT (Year, Month, Day)	15. PAGE COUNT
Final Report	FROM Mar 82 TO Dec 84	1986 June	85

16. SUPPLEMENTARY NOTATION

17.	COSATI CODES		18. SUBJECT TERMS (Continue on reverse if necessary and identify by block number)
FIELD	GROUP	SUB-GROUP	antenna coupling; gain; mutual gain; spherical angular functions; microwave; reflector; near-field; far-field; antenna pattern; stationary phase

19. ABSTRACT (Continue on reverse if necessary and identify by block number)

Theoretical and numerical analyses were performed to develop a computer algorithm for computing antenna mutual gain for arbitrary arrangements and orientations of antennas located in the near-field of each other and operating in the presence of near-field scattering obstacles. The mathematical expressions and algorithm were developed based on the use of the complex far-field electric field data for each antenna. The algorithm, designated as GTSAF, has been implemented and employed to generate coupling data for directive aperture antennas operating (1) on a clear site, and (2) in the presence of a scattering obstacle. Coupling data for a pair of short dipoles has also been generated via GTSAF, and compared with numerical data obtained via the Method of Moments (MOM).

20 DISTRIBUTION/AVAILABILITY OF ABSTRACT	21. ABSTRACT SECURITY CLASSIFICATION
☑ UNCLASSIFIED/UNLIMITED ☐ SAME AS RPT. ☐ DTIC USERS	Unclassified

22a. NAME OF RESPONSIBLE INDIVIDUAL	22b. TELEPHONE (Include Area Code)	22c. OFFICE SYMBOL
Stuart Albert	(201) 544-5359	AMSEL-COM-AY-2

DD FORM 1473, 84 MAR 83 APR edition may be used until exhausted. SECURITY CLASSIFICATION OF THIS PAGE
All other editions are obsolete. UNCLASSIFIED

TABLE OF CONTENTS

A-1

iii

LIST OF FIGURES

LIST OF TABLES

FOREWORD

The research on this program was performed by personnel of the
Electromagnetic Effectiveness Division of the Electronics and Computer
Systems Laboratory of the Engineering Experiment Station at the Georgia
Institute of Technology, Atlanta, Georgia 30332. Dr. Barry J. Cown served
as the Project Director. This program was sponsored by the U.S. Army
Communications-Electronics Command (CECOM), Ft. Monmouth, New Jersey,
07703, and is designated by Georgia Tech as Project A-3213. This Final
Technical Report covers the period from March 29, 1982 through December 31,
1984. The report summarizes the key results obtained during this period
and is required by the contract. Technical discussions with and
suggestions by the Technical Monitor, Mr. Stuart Albert of CECOM are
gratefully acknowledged. The authors also cite the considerable clerical
skills of Ms. Mercedes Saghini and Lois R. Savvoir in preparing this
report.

Respectfully submitted,

Barry J. Cown
Project Director

Approved:

Charles E. Ryan, Jr.
Chief,
EM Effectiveness Division

SECTION I

INTRODUCTION

The results for this research program are summarized in this Final
Technical Report. The primary goal of this research effort was to develop
an efficient, flexible computer algorithm for computing the coupling
between pairs of Army antennas. Emphasis was placed on the development of
a practical algorithm for analyzing the coupling between pairs of directive
antennas when both antennas are operating within their design frequency
bands and are located within the near field of each other. The effects of
scattering from nearby support structures and other antennas on antenna
coupling were also addressed in this research program. Clearly, the
electromagnetic coupling analysis of Army antennas must be based on
analytical techniques that are efficient and accurate for analyzing near-
field coupling and scattering phenomena. The analytical techniques should
also be flexible enough to permit extension to handle coupling analysis
over wide frequency bands at both in-band and out-of-band frequencies.
Although major emphasis was given to coupling between directive antennas
under both "clear-site" conditions and "partially-obstructed" conditions,
the coupling model described herein is also applicable to antennas of
moderate or low directivity.

One can readily identify several basic methods that have been applied
to the analysis of antenna coupling for restricted classes of antennas.
These are the Method of Moments (MOM) [1,2] , Aperture Integration (AI)
[3,4], the Geometrical Theory of Diffraction (GTD) [5-7], and the Plane
Wave Spectrum (PWS) analysis [8-11]. Methods based on a spherical harmonic
wave expansions have also been formulated for computing clear-site coupling
[10,11]. Finally, a method based on the Spherical Angular Functions (SAF)
for the antennas and scattering obstacles was developed on this contract [12].

The MOM is efficient for computation of coupling between electrically-
small (low directivity) antennas operating on a clear-site or operating in
the presence of electrically-small scattering obstacles. The MOM cannot be
economically applied to antennas of moderate or high directivity due to the
excessive number of wire elements required for accurate modeling. The AI

1

and GTD methods have been applied in the analysis of electrically-large (directive) antennas, and the GTD has also been applied to electrically-small antennas mounted on vehicles and aircraft. However, the AI and GTD methods require recomputation of the electric fields in the near-field whenever either antenna is rotated or when either antenna or obstacle locations are changed.

The PWS analysis overcomes many of the disadvantages of the AI and the GTD analyses for directive antennas whose locations/orientations are varied. In general, spectral analysis techniques are particularly well suited for efficient and accurate characterization of a wide variety of near-field coupling and scattering phenomena involving electrically-large antennas and/or scattering objects. To date, the PWS analysis has been employed to analyze the effects of near-field scattering obstacles on antenna performance for a wide variety of situations that would be comparatively awkward and less efficient to analyze via the Method of Moments (MOM), aperture integration and/or the Geometrical Theory of Diffraction (GTD). The PWS analysis has also been applied to analyze the coupling between a pair of near-field directive antennas, under both "clear-site" conditions [8-11] and with an intervening metal cylinder located between them [10]. The success of the PWS analysis for numerical analysis of near-field coupling and scattering for directive antennas and scattering obstacles is due largely to the speed of the Fast Fourier Transform (FFT) that is employed when the integrations over the transverse wavenumbers $\bar{k}_t$ are confined to "visible space" limits $|\bar{k}_t| \leq k_o$ ($k_o = 2\pi/\lambda$, where λ is the wavelength) [13].

It is important to distinguish between the rigorous Plane Wave Spectrum analysis presented by Kerns [14] and the approximate analysis that is used in practice. In practice, researchers typically work only with the PWS over a portion of the "forward" hemisphere and ignore the propagating electromagnetic fields at wide angles in the front hemisphere and the "evanescent" fields in the "invisible" space. This procedure has proven to give accurate results when the coupling or scattering integral over the excluded energy is small compared to the corresponding integrals over the included energy, as is the case for many coupling or scattering situations involving directive antennas and scatterers.

2

There are some potential difficulties associated with the approximate PWS analysis for certain commonly-encountered orientations of closely-spaced antennas/scatterers for situations where one of the antennas, both of the antennas, or one or more of the scattering obstacles have low directivity. Consider first the situation depicted in Figure 1-1 for two directive antennas. The PWS analysis is readily applied to the coupling situation depicted in Figure 1-1 for both the clear site situation shown in the figure, as well as with a directive scattering obstacle located anywhere between the two antennas, provided the rotation angles are not "too large". When the antennas are closely-spaced and the peak of the mainbeam approaches to within about 2 or 3, 3-dB beamwidths of 90 degrees, it may be necessary to extend the PWS coupling integral integration limits beyond the usual "visible space" limits $|\overline{k}_t| = k_o$. Although this procedure is analytically straightforward, it can be inconvenient numerically because it would be necessary (1) to compute the PWS spectrum functions for $|\overline{k}_t| >$ k_o and (2) to compute the coupling integral which has a numerical singularity in the integrand at $|\overline{k}_t| = k_o$. Alternatively, one could possibly choose a new plane centered on the line joining the centers of the two antennas, or perhaps two or more "canted" planes which allow one to avoid using portions of k-space for $|\overline{k}_t| \geq k_o$. However, values of coupling computed numerically for closely spaced antennas may be sensitive to the choice of canted planes and to numerical "filters" that are employed, deliberately or inadvertently, in the computer processing. The practical concerns just described are even more cogent for arbitrary coupling situations such as the one shown in Figure 1-2 for two directive antennas, and for antennas of low directivity in general. In fact, the coupling situation depicted in Figure 1-2 probably occurs more frequently at Army field sites than does the one depicted in Figure 1-1, since care is ordinarily taken to avoid pointing the mainbeam of an antenna in the general direction toward a susceptible antenna.

In light of the foregoing considerations, an alternative analysis referred to as the Spherical Angular Function (SAF) analysis has

3
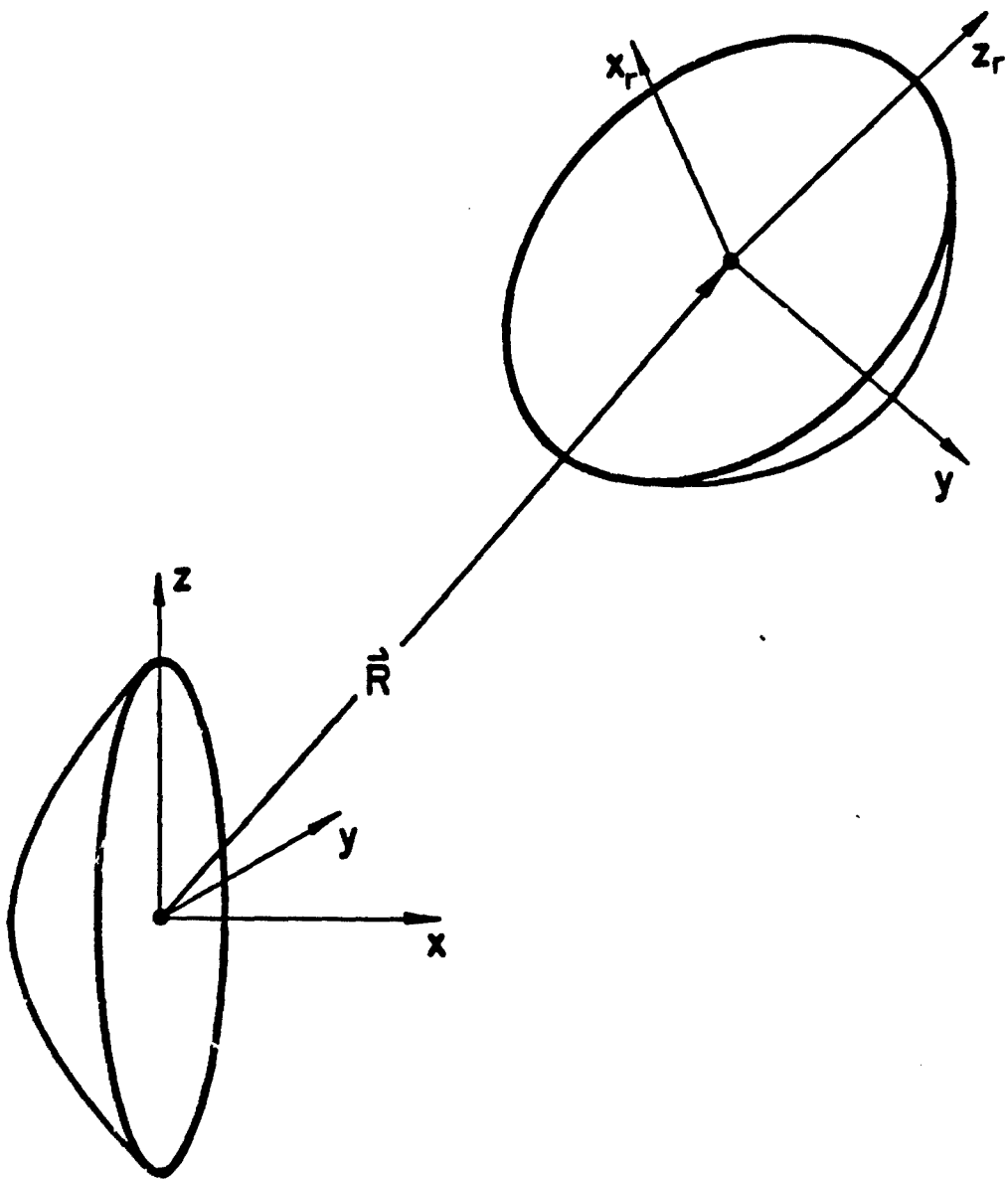
Figure 1-1.   Sketch depicting the arrangement of two antennas appropriate
              for the PWS analysis of coupling.
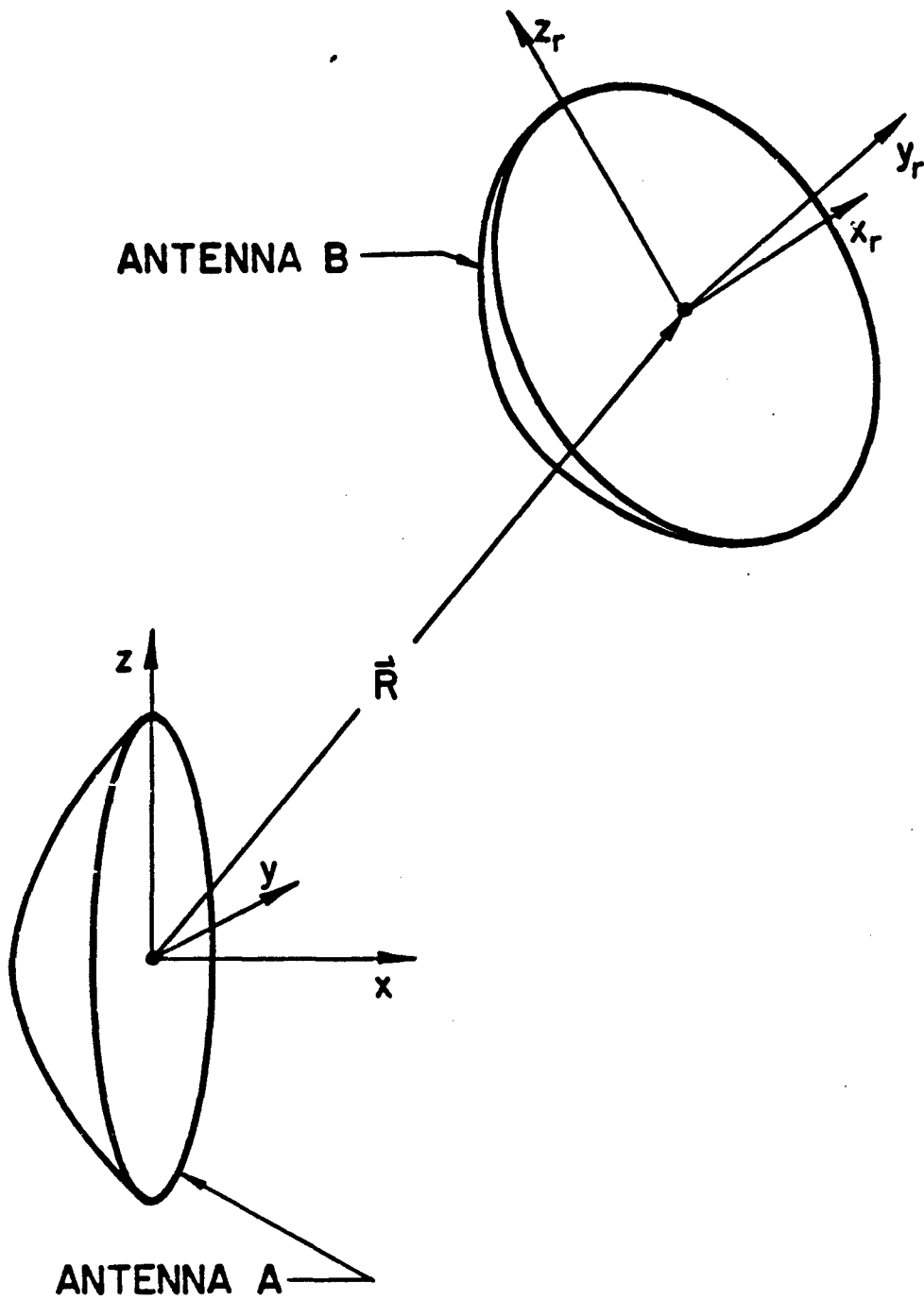
Figure J-2.   Sketch depicting two arbitrarily oriented near-field
             antennas and geometric parameters.

been formulated to accurately compute coupling data for arbitrary antenna arrangements.

Based on the technical considerations mentioned in the preceeding paragraphs, the approach that was taken to achieve the overall objective stated in the first paragraph consisted of the following two major tasks:

TASK 1: Theoretical and numerical investigations of the Spherical Angular Function coupling analysis were performed (1) to develop the theory and equations for analysis of arbitrary antenna arrangements and (2) to derive suitable approximate coupling equations for EMC engineering applications that employ the use of selected subsets of the full spherical angular spectrum.

TASK 2: Based on the results of Tasks 1 and 2, a practical, user-oriented antenna coupling algorithm for application to Army antennas was developed and implemented.

The theory and equations for the rigorous SAF are presented and discussed in Section II. Useful approximate analyses and equations are presented in Section III. Illustrative antenna coupling curves computed via computer algorithm GTSAF and auxiliary programs are presented and discussed in Section IV. Concluding remarks and recommendations are contained in Section V.

SECTION II
SPHERICAL ANGULAR FUNCTION ANTENNA ANALYSIS

A. Introduction

A coupling analysis is sought which is readily applied to arbitrary orientations and arrangements of antennas located within the near-field of each other. No restrictions are made concerning the directivity of the antennas. Multiple scattering among the antennas is ignored in the analysis presented herein. The coupling analysis is first conduced for antennas that are operating on a "clear site" free from scattering structures. The coupling analysis is then extended to handle effects of scattering from obstacles that are located within the near-field of the antennas.

The coupling analysis described herein employs the Spherical Angular Functions (SAF) of each antenna. The SAF, denoted as $\bar{F}(\theta, \phi)$, is related to the far-field electric field $E_{ff}(\theta, \phi)$ by the equation

$$\bar{E}_{ff}(\theta, \phi) = \frac{e^{-jkr}}{r} \bar{F}(\theta, \phi) \tag{2-1}$$

where (r, θ, ϕ) are the range, elevation angle, and azimuth angle of a selected point in the far-field region of the antenna. Hence, $\bar{F}(\theta, \phi)$ is then

$$\bar{F}(\theta, \phi) = re^{+jkr} \bar{E}_{ff}(\theta, \phi) \tag{2-2}$$

where we note that $\bar{E}_{ff}(\theta, \phi)$ and, hence, $\bar{F}(\theta, \phi)$ are analytic over the entire far-field sphere for any realizable antenna. This is a desirable property since the analysis is based on a coupling integral involving a convolution of the SAF's for the two antennas integrated over the entire far-field sphere. The theory and equations for the SAF analysis are presented and discussed in Subsections B and C for antennas operating on a clear site. The theory and equations for antennas operating in the presence of near-field obstacles are summarized in Subsection D.

B. Coordinate Space Coupling Integral

A convenient starting point for the analysis is the "reaction", or

7

"coupling", integral due to Rumsey [15]. The coupling integral, denoted as $((b,a))$, is equal to the open circuit voltage V^{ba} induced in the "terminals" of the receiving Antenna B by the transmitting Antenna A. The terminals referred to here can be, for example, the gap between the inner and outer conductors of a coax-to-waveguide feed, or a coupling iris, or a selected "terminal plane" inside the waveguide. The coupling integral given as Equation 49 of Reference 15 is written here as the surface integral

$$V^{ba} = ((b,a)) =$$

$$- \iint_{S'} [\ \bar{E}^a(\bar{R}+\bar{r}') \times \bar{H}^b(\bar{r}') + \bar{H}^a(\bar{R}+\bar{r}') \times \bar{E}^b(\bar{r}')] \cdot \hat{n}' \ ds'] \qquad (2\text{-}3)$$

where S' is an arbitrary surface enclosing Antenna B and $\hat{n}'$ is a unit vector normal to the surface and pointing outward, as shown in Figure 2-1.

$\bar{E}^a$ and $\bar{H}^a$ are the electric field and the magnetic field "intensity" produced by Antenna A on the surface S'. The interpretation of $\bar{E}^b$ and $\bar{H}^b$ depends on whether the receiving antenna, Antenna B, contains gyrotropic material [16].

If Antenna B does not contain any gyrotropic material, $\bar{E}^b$ and $\bar{H}^b$ are the fields that Antenna B would establish on the surface S' when used as a transmitter with unit input current. In this case, the transmitting and receiving patterns are said to be equal. More precisely, the transmitted complex fields $\bar{E}^b$ and $\bar{H}^b$ established at a point $\bar{r}'$ are proportional to the complex voltage response of the antenna when used as a receiver with an idealized infinitesimal dipole source located at $\bar{r}'$. If Antenna B contains gyrotropic material, such as a ferrite device, $\bar{E}^b$ and $\bar{H}^b$ are the fields established on the surface S' with a unit input current and with the direction of the applied magnetic field reversed from the direction normally used during transmission. In this case, the receiving pattern is said to be equal to the "transpose" transmitting pattern. More precisely, the transmitted fields $\bar{E}^b$ and $\bar{H}^b$ established when the biasing magnetic field is reversed through the ferrite are proportional to the voltage response when the antenna is used as a receiver with idealized

8
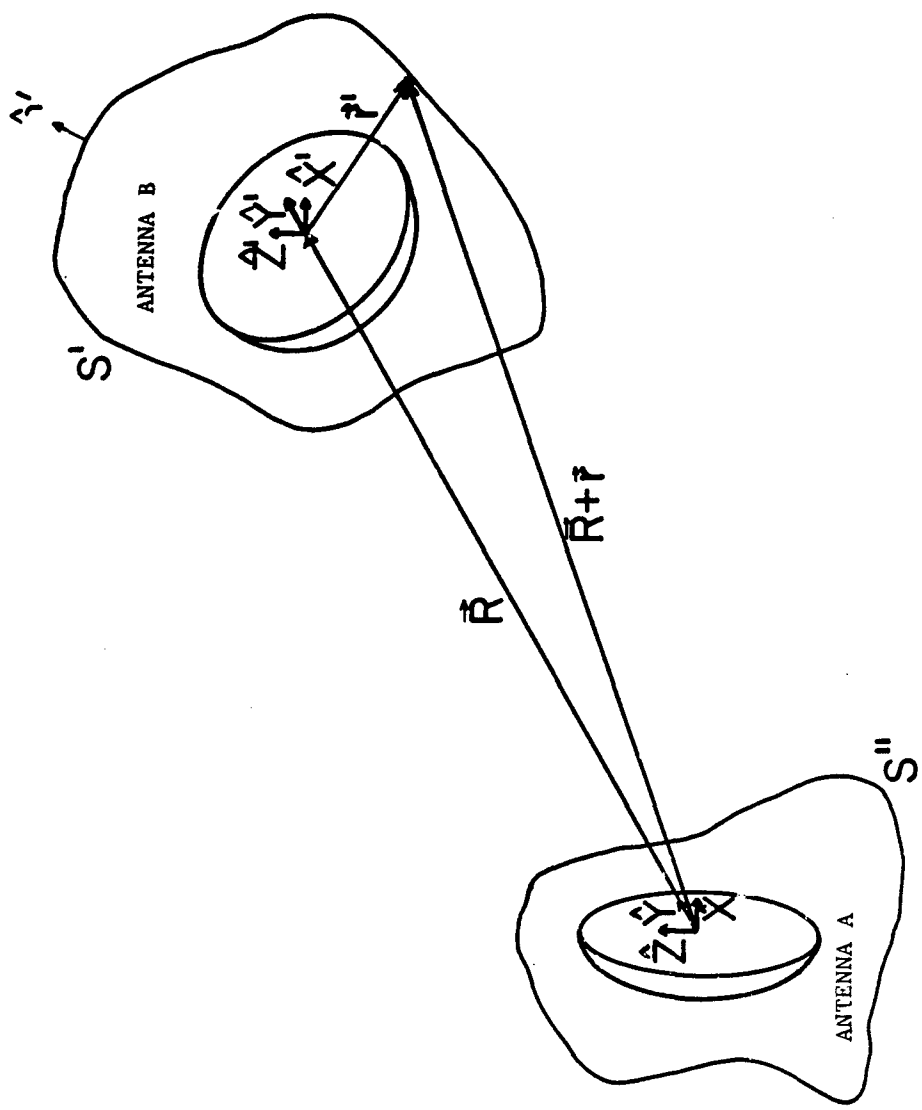
Figure 2-1. Sketch depicting antenna site coordinate systems and arbitrary enclosing surfaces used in the mathematical analysis.

infinitesimal dipole source located at $\bar{r}'$ and the biasing magnetic field
applied in the direction for normal operation.

The polarization states of the two antennas must be specified with
respect to a chosen coordinate system in order to perform the vector
operations indicated in the integrand of the coupling integral. If the
polarization of each antenna is resolved in cartesian components with
respect to non-rotating, parallel cartesian coordinates fixed at the center
of rotation of each antenna, the vector operations will be independent of
the relative location of the antennas. However, the vector operations will
be functions of relative rotation angles of the antennas. If the antenna
polarizations are each resolved in terms of spherical components with
respect to the parallel, non-rotating cartesian coordinate system at the
centers of rotation of the two antennas, the vector operations will depend
on both the relative location and the antenna rotation angles. However,
the vector operations can be readily performed via spherical transformation
and rotation matrices. The computer program will be designed to compute
coupling versus relative orientation angles for a fixed relative location
of the two antennas. Consequently, spherical polarization components are
selected.

Antenna patterns are customarily recorded and/or computed for (θ, ϕ)
polarizations. The r-polarized components of $\bar{E}$ and $\bar{H}$ can be expressed in
terms of the (θ, ϕ) components via the Maxwell curl relations

$$\bar{E} = \frac{1}{j\omega\epsilon} \ (\bar{\nabla} \times \bar{H}), \text{ and} \tag{2-4}$$

$$\bar{H} = -\frac{1}{j\omega\mu} \ (\bar{\nabla} \times \bar{E}) \tag{2-5}$$

which lead to the equations

$$E_r\hat{r} = \frac{1}{j\omega\epsilon} \hat{r} \ \frac{1}{r\sin\theta} \ \frac{\partial}{\partial\theta} \ (H_\phi\sin(\theta) - \frac{\partial H_\theta}{\partial\phi}) \tag{2-6}$$

$$H_r\hat{r} = -\frac{1}{j\omega\mu} \hat{r} \ \frac{1}{r\sin\theta} \ \frac{\partial}{\partial\theta} \ (E_\phi\sin(\theta) - \frac{\partial E_\theta}{\partial\phi}) \tag{2-7}$$

respectively. The $\hat{r}$ component can be neglected in many practical antenna

10

coupling situations, but we shall retain it in the theory and equations for the sake of completeness.

The spherical polarization components of Antenna A and Antenna B may be written as

$$\begin{bmatrix} \hat{\theta} \\ \hat{\phi} \\ \hat{r} \end{bmatrix} = \begin{bmatrix} \cos(\tilde{\theta})\cos(\tilde{\phi}) & \cos(\theta)\sin(\tilde{\phi}) & -\sin(\tilde{\theta}) \\ -\sin(\tilde{\phi}) & \cos(\tilde{\phi}) & 0 \\ \sin(\tilde{\theta})\cos(\tilde{\phi}) & \sin(\tilde{\theta})\sin(\tilde{\phi}) & \cos(\tilde{\phi}) \end{bmatrix} \begin{bmatrix} \hat{x} \\ \hat{y} \\ \hat{z} \end{bmatrix}$$

$$, \text{ and} \qquad (2\text{-}8)$$

$$\begin{bmatrix} \hat{\theta}' \\ \hat{\phi}' \\ \hat{r}' \end{bmatrix} = \begin{bmatrix} \cos(\tilde{\theta}')\cos(\tilde{\phi}') & \cos(\tilde{\theta}')\sin(\tilde{\phi}') & -\sin(\tilde{\theta}') \\ -\sin(\tilde{\phi}') & \cos(\tilde{\phi}') & 0 \\ \sin(\tilde{\theta}')\cos(\tilde{\phi}') & \sin(\tilde{\theta}')\sin(\tilde{\phi}') & \cos(\tilde{\phi}') \end{bmatrix} \begin{bmatrix} \hat{x}' \\ \hat{y}' \\ \hat{z}' \end{bmatrix}$$

$$(2\text{-}9)$$

respectively. The $\sim$ symbol is placed over the near-field θ and ϕ variables to distinguish them from far-field angular variables that will be presented later. The $(\hat{x}, \hat{y}, \hat{z})$ and $(\hat{x}', \hat{y}', \hat{z}')$ are parallel non-rotating cartesian unit vectors fixed at the center of rotation of Antenna A and Antenna B, respectively. The angles $\tilde{\theta}$ and $\tilde{\phi}$ for Antenna A may be expressed as functions of the angles $\tilde{\theta}'$ and $\tilde{\phi}'$ for a point on the surface enclosing Antenna B. In particular, the expressions for $\sin(\tilde{\theta})$ and $\sin(\tilde{\phi})$ are

$$\sin(\tilde{\theta}) = \left[1 - \left[\frac{R\cos(\theta_o) + r'\cos(\tilde{\theta}')}{|\bar{R} + \bar{r}'|} \right]^2 \right]^{1/2} \quad , \text{ and} \qquad (2\text{-}10)$$

$$\sin(\tilde{\phi}) = \frac{R\sin(\theta_o)\sin(\phi_o) + r'\sin(\tilde{\theta}')\sin(\tilde{\phi}')}{|\bar{R} + \bar{r}'|\sin(\tilde{\theta})} \qquad (2\text{-}11)$$

We note here that the conditions that make $\sin(\tilde{\theta})$ equal to zero also cause

11

the numerator of Equation (2-11) to equal zero. More precisely, the numerator and denominator of Equation (2-11) both approach zero as $\sin(\tilde{\theta})$ approaches zero and the proper limiting value of Equation (2-11) is zero.

The projection of the polarization components of Antenna A onto the surface enclosing Antenna B can be accomplished via the transformation matrix [T], to wit:

$$
\begin{bmatrix} E^a_{\theta'} \\ E^a_{\phi'} \\ E^a_{r'} \end{bmatrix} = \begin{bmatrix} T_{\theta\theta'} & T_{\phi\theta'} & T_{r\theta'} \\ T_{\theta\phi'} & T_{\phi\phi'} & T_{r\phi'} \\ T_{\theta r'} & T_{\phi r'} & T_{rr'} \end{bmatrix} \begin{bmatrix} E^a_{\theta} \\ E^a_{\phi} \\ E^a_{r} \end{bmatrix}
$$

(2-12)

The elements of [T] are computed by forming the scalar product of the subscripted unit vectors. For example, $T_{\theta\theta'} = \hat{\theta}' \cdot \hat{\theta}'$, $T_{\phi r'} = \hat{\phi} \cdot \hat{r}'$, and so forth. The elements are tabulated in Table 2-1 for convenience.

The vector operations contained in the integrand of the coupling integral can now be performed with the aid of Equations (2-6) through (2-12). Let the surface enclosing the receiving antenna be a sphere of radius r'. Thus, the unit normal $\hat{n}'$ to the surface is then identical with $\hat{r}'$. Consequently, only the $\hat{r}'$ component of the vector cross product terms within the square brackets of the integrand survive when the scalar product is formed with $\hat{r}'$. The coupling integral is written as the sum of four integrals,

$$
V^{ba} = -((E^a_{\theta'}, H^b_{\phi'})) + ((E^a_{\phi'}, H^b_{\theta'})) - ((H^a_{\theta'}, E^b_{\phi'})) + ((H^a_{\phi'}, E^b_{\theta'}))
$$

(2-13)

where the integrals are

$$
((E^a_{\theta'}, H^b_{\phi'})) = \iint_{S'} [E^a_{\theta}(\bar{R}+\bar{r}')\, T_{\theta\theta'} + E^a_{\phi}(\bar{R}+\bar{r}')\, T_{\phi\theta'}
$$

$$
+ E^a_{r}(\bar{R}+\bar{r}')\, T_{r\theta'}]\, H^b_{\phi'}(\bar{r}')\, ds',
$$

(2-14)

12

TABLE 2-1

MATHEMATICAL EXPRESSIONS FOR THE ELEMENTS OF THE POLARIZATION

TRANSFORMATION MATRIX $[T]$

Matrix Element	Definition	Expression
$T_{\theta\theta'}$	$\hat{\theta} \cdot \hat{\theta}'$	$\cos(\tilde{\theta})\cos(\tilde{\phi})\cos(\tilde{\theta}')\cos(\tilde{\phi}') + \cos(\tilde{\theta})\sin(\tilde{\phi})\cos(\tilde{\theta}')\sin(\tilde{\phi}') + \sin(\tilde{\theta})\sin(\tilde{\theta}')$
$T_{\theta\phi'}$	$\hat{\theta} \cdot \hat{\phi}'$	$-\cos(\tilde{\theta})\cos(\tilde{\phi})\sin(\tilde{\phi}') + \cos(\tilde{\theta})\sin(\tilde{\phi})\cos(\tilde{\phi}')$
$T_{\theta r'}$	$\hat{\theta} \cdot \hat{r}'$	$\cos(\tilde{\theta})\cos(\tilde{\phi})\sin(\tilde{\theta}')\cos(\tilde{\phi}') + \cos(\tilde{\theta})\sin(\tilde{\phi})\sin(\tilde{\theta}')\sin(\tilde{\phi}') - \sin(\tilde{\theta})\cos(\tilde{\phi}')$
$T_{\phi\theta'}$	$\hat{\phi} \cdot \hat{\theta}'$	$-\sin(\tilde{\phi})\cos(\tilde{\theta}')\cos(\tilde{\phi}') + \cos(\tilde{\phi})\cos(\tilde{\theta}')\sin(\tilde{\phi}')$
$T_{\phi\phi'}$	$\hat{\phi} \cdot \hat{\phi}'$	$\sin(\tilde{\phi})\sin(\tilde{\phi}') + \cos(\tilde{\phi})\cos(\tilde{\phi}')$
$T_{\phi r'}$	$\hat{\phi} \cdot \hat{r}'$	$-\sin(\tilde{\phi})\sin(\tilde{\theta}')\cos(\tilde{\phi}') + \cos(\tilde{\phi})\sin(\tilde{\theta}')\sin(\tilde{\phi}')$
$T_{r\theta'}$	$\hat{r} \cdot \hat{\theta}'$	$\sin(\tilde{\theta})\cos(\tilde{\phi})\cos(\tilde{\theta}')\cos(\tilde{\phi}') + \sin(\tilde{\theta})\sin(\tilde{\phi})\cos(\tilde{\theta}')\sin(\tilde{\phi}') - \cos(\tilde{\phi})\sin(\tilde{\theta}')$
$T_{r\phi'}$	$\hat{r} \cdot \hat{\phi}'$	$-\sin(\tilde{\theta})\cos(\tilde{\phi})\sin(\tilde{\phi}') + \sin(\tilde{\theta})\sin(\tilde{\phi})\cos(\tilde{\phi}')$
$T_{rr'}$	$\hat{r} \cdot \hat{r}'$	$\sin(\tilde{\theta})\cos(\tilde{\phi})\sin(\tilde{\theta}')\cos(\tilde{\phi}') + \sin(\tilde{\theta})\sin(\tilde{\phi})\sin(\tilde{\theta}')\sin(\tilde{\phi}') + \cos(\tilde{\phi})\cos(\tilde{\phi}')$

13

$$\left(\!\left(E^a_{\phi'}, H^b_{\theta'} \right)\!\right) = \iint_{S'} [E^a_\theta (\bar{R}+\bar{r}')\, T_{\theta\phi'} + E^a_\phi (\bar{R}+\bar{r}')\, T_{\phi\phi'}$$

$$+ E^a_r (\bar{R}+\bar{r}')\, T_{r\phi'}]\, H^b_\theta (\bar{r}')\, ds',$$

<div align="right">(2-15)</div>

$$\left(\!\left(H^a_{\theta'}, E^b_{\phi'} \right)\!\right) = \iint_{S'} [H^a_\theta (\bar{R}+\bar{r}')\, T_{\theta\theta'} + H^a_\phi (\bar{R}+\bar{r}')\, T_{\phi\theta'}$$

$$+ H^a_r (\bar{R}+\bar{r}')\, T_{r\theta'}]\, E^b_\phi (\bar{r}')\, ds', \quad \text{and}$$

<div align="right">(2-16)</div>

$$\left(\!\left(H^a_{\phi'}, E^b_{\theta'} \right)\!\right) = \iint_{S'} [H^a_\theta (\bar{R}+\bar{r}')\, T_{\theta\phi'} + H^a_\phi (\bar{R}+\bar{r}')\, T_{\phi\phi'}$$

$$+ H^a_r (\bar{R}+\bar{r}')\, T_{r\phi'}]\, E^b_\theta (\bar{r}')\, ds' .$$

<div align="right">(2-17)</div>

These integrals express the coupling in terms of the spherical polarization components of the near-field $\bar{E}$ and $\bar{H}$ fields of the two antennas and the components of a spherical polarization transformation matrix. Similar expressions can be derived for cartesian polarization components, but they are not needed in this analysis.

C. SAF Coupling

The integrals (2-14) through (2-16) require the use of the near-field $\bar{E}$ and $\bar{H}$ fields of the two antennas to compute coupling. The near-field $\bar{E}$- and H-fields for most antennas are not ordinarily known. They can, of course, be measured or they can be computed from the known far-field quantities. Thus, considerable time and money resources would have to be devoted to obtain the near-field data. Then one still has to perform the integrations (2-14) through (2-17). Thus, it will be advantageous to express the integrals in terms of the far-field $\bar{E}$ and $\bar{H}$ fields of the antenna.

Each of the four coupling integrals (2-14) through (2-17) is the sum of three coupling integrals, all of which have the same general form. In

<div align="center">14</div>

particular, the coupling integral $((E_{\theta'}^a, H_{\theta}^b))$ may be written as

$$((E_\theta^a, H_{\phi'}^b)) = ((E_\theta^a T_{\theta\theta'}, H_{\phi'}^b)) + ((E_\theta^a T_{\phi\theta'}, H_{\phi'}^b)) + ((E_r^a T_{r\theta'}, H_{\phi'}^b))$$

Attention is focused on $((E_\theta^a T_{\theta\theta'}, H_{\phi'}^b))$ which is typical of the integrals under consideration. This integral is

$$((E_\theta^a T_{\theta\theta'}, H_{\phi'}^b)) = \iint\limits_{S'} E_\theta^a(\bar{R}+\bar{r}') H_{\phi'}^b(\bar{r}_\theta') T_{\theta\theta'} \, ds'.$$

$$(2\text{-}18)$$

Since the surface has been chosen to be a sphere of radius r' centered on Antenna B, this can be written more explicitly as

$$((E_\theta^a T_{\theta\theta'}, H_{\phi'}^b)) = (r')^2 \int\limits_{o}^{\pi}\int\limits_{-\pi}^{\pi} E_\theta^a(\bar{R}+\bar{r}') H_{\phi'}^b(\bar{r}') T_{\theta\theta'} \, \sin(\theta')d\phi'd\theta'$$

$$(2\text{-}19)$$

where it should be noted that $T_{\theta\theta'}$ is also a function of r' and the integration variables (θ', ϕ').

The integrals (2-18) or (2-19) belong to a class of generalized convolution integrals defined on an arbitrary closed surface. The generalized convolution integral is

$$C^{\pm}(\bar{R}) = \iint\limits_{S'} \bar{A}(\bar{R}\pm\bar{r}') \cdot \bar{B}(\bar{r}')ds'$$

$$(2\text{-}20)$$

where the notion of convolution has been extended to include integrands involving $\bar{A}(\bar{R}+\bar{r}') \cdot \bar{B}(\bar{r}')$ as well as the usual $\bar{A}(\bar{R}-\bar{r}') \cdot \bar{B}(\bar{r}')$. Integrands of the type $\bar{A}(\bar{r}'-\bar{R}) \cdot \bar{B}(\bar{r}')$ can also be included, but they are not needed here. The generalized convolution integral $C^{\pm}(\bar{R})$ has the useful property

$$\iint\limits_{S'} \bar{A}(\bar{R}\pm\bar{r}') \cdot \bar{B}(\bar{r}')ds' = \frac{1}{2\pi^2} \iiint\limits_{\Gamma_\kappa} \frac{\exp[\mp j\bar{\kappa}\cdot\bar{R}]}{\kappa^2 - k^2} \bar{a}(\bar{\kappa})\cdot\bar{b}(\bar{\kappa})d\Gamma_\kappa$$

$$(2\text{-}21)$$

15

where

$$\bar{a}(\bar{\kappa}) = \frac{1}{4}\pi \iint\limits_{S''} [\bar{A}(\bar{r}'') \frac{\partial}{\partial n} - \frac{\partial \bar{A}(\bar{r}'')}{\partial n}] \, e^{j\bar{\kappa}\cdot\bar{r}''} \, d\bar{s}'', \text{ and} \quad (2\text{-}22)$$

$$\bar{b}(\bar{\kappa}) = \iint\limits_{S'} \bar{B}(\bar{r}')e^{\pm j\bar{\kappa}\cdot\bar{r}'} \, ds'. \quad (2\text{-}23)$$

$\frac{\partial}{\partial n}$ is the normal derivative on the surface S" where S" is a surface enclosing the sources of $\bar{A}$, S' is a surface enclosing the sources of $\bar{B}$, $\bar{\kappa}$ is a wavevector, and Γ_κ is a three-dimensional volume in wavevector space.

The relation (2-21) holds under conditions that are much less restrictive than those encountered in real-world antenna coupling and scattering problems. Sufficiency conditions for (2-21) are (1) the vector fields $\bar{A}$ and $\bar{B}$ each satisfy the homogeneous vector Helmholtz equation outside their respective source regions, (2) the sources of $\bar{A}$ are contained inside a finite surface s_a < S" and the sources of $\bar{B}$ are contained inside a finite surface s_b < S', and (3) S' and S" do not overlap.

The derivation of (2-21) is readily accomplished under the conditions just stated. The field $\bar{A}$ ($\bar{R}+\bar{r}'$) can be expressed as the Huygens-Fresnel integral [17]

$$\bar{A}(\bar{R}+\bar{r}') = \frac{1}{4\pi} \iint\limits_{S''} [\bar{A}(\bar{r}'') \frac{\partial}{\partial n} - \frac{\partial \bar{A}(\bar{r}'')}{\partial n}] \, G(\bar{R}+\bar{r}' \,|\, \bar{r}'') \, d\bar{r}'', \quad (2\text{-}24)$$

where $\frac{\partial}{\partial n}$ denotes the normal derivative at the surface S" and where G is the free space Green's function given as

$$G(\bar{R}+\bar{r}' \,|\, \bar{r}'') = \frac{\exp[-jk\,|(\bar{R}+\bar{r}')-\bar{r}''|\,]}{|(\bar{R}+\bar{r}')-\bar{r}''|} \quad (2\text{-}25)$$

16

Next, the coordinate space representation of G is replaced by the wavevector space, or spectral, representation G_k given as

$$G_k(\bar{R} + \bar{r}' \mid \bar{r}'') = \frac{1}{2\pi^2} \iiint_{\Gamma_k} \frac{\exp[-j\bar{\kappa}\cdot(\bar{R}+\bar{r}'-\bar{r}'')]}{\kappa^2-k^2} \, d\Gamma_\kappa \qquad (2\text{-}26)$$

where Γ_κ is a three-dimensional volume in wavevector space[18]. The "shape" of Γ_κ and the integration limits will be specified shortly. If G_k is substituted into (2-24), and (2-24) is substituted into (2-20), we arrive at the expression

$$C^{\pm}(\bar{R}) = \frac{1}{2\pi^2} \iiint_{\Gamma_\kappa} \frac{\exp[\mp j\bar{\kappa}\cdot\bar{R}]}{\kappa^2-k^2} \left\{ \frac{1}{4\pi} \iint_{S''} [\bar{A}(\bar{r}') \frac{\partial}{\partial r} - \frac{\partial \bar{A}(\bar{r}'')}{\partial r}] \exp[j\bar{\kappa}\cdot\bar{r}''] \, ds'' \right.$$

$$\left. \iint_{S'} \bar{B}(\bar{r}') \exp[\mp j\bar{\kappa}\cdot\bar{r}'] \, ds' \right\} d\Gamma_\kappa , \qquad (2\text{-}27)$$

which is equal to the right-hand side of (2-21). The order of the integration was interchanged in arriving at (2-27). This is permissible because the integrands involving $\bar{A}$ and $\bar{B}$ are "square integrable" over their respective domains. The integrands involving $\bar{A}$ and $\bar{B}$ are square integrable because they are produced by sources of finite extent. For the integral over Γ_κ, a contour which circumvents the simple poles of the wavevector integral located at $\kappa = \pm k$ is chosen in order to properly represent the Green's function (2-25). The wavevector integrand is finite and integrable along the specified path.

It will be advantageous to use the spherical integral representation of the Green's function given as [18,19]

$$G(\bar{R}+\bar{r}' \mid \bar{r}'') = \frac{1}{4\pi^2} \int_{-\infty}^{\infty} \int_{0}^{\pi} \int_{-\pi}^{\pi} \frac{\exp[-j\bar{\kappa}\cdot(\bar{R}+\bar{r}'-\bar{r}'')]}{\kappa^2-k^2} \, \kappa^2 \sin\theta d\phi d\theta d\kappa . \qquad (2\text{-}28)$$

17

where the integration over κ follows the contours shown in Figure 2-2. Thus, the path of integration is along contour C_1 for $\cos(\gamma) < 0$ and along countour C_2 for $\cos(\gamma) > 0$, where γ denotes the angle between $\bar{\kappa}$ and $\bar{R}$. Since functions $a(\bar{\kappa})$ and $b(\bar{\kappa})$ are analytic, the only poles are the ones at $\kappa = \pm k$. Hence, application of the residue calculus to Equation (2-27) yields

$$C^{\pm}(\bar{R}) = k \int_{0}^{\pi} \int_{-\pi}^{\pi} \exp[-j\bar{k}(\theta,\phi) \cdot \bar{R}] \, \bar{a}(\theta,\phi) \cdot \bar{b}(\theta,\phi) \sin\theta \, d\phi \, d\theta \tag{2-29}$$

where

$$\bar{k}(\theta,\phi) = k_o \sin(\theta)\cos(\phi) \, \hat{x} + k_o \sin(\theta)\sin(\phi) \, \hat{y} + k_o \cos\theta \hat{z} \tag{2-30}$$

This result is, of course, applicable to each scalar component $\bar{a} \cdot \bar{b}$ of the integrand.

The partial coupling integral of Equation (2-19) can be expressed with the aid of Equation (2-29) as

$$\langle\!\langle E_{\theta}^{a} T_{\theta\theta'}, H_{\phi}^{b} \rangle\!\rangle = k \int_{0}^{\pi} \int_{-\pi}^{\pi} \exp[-j\bar{k}(\theta,\phi) \cdot \bar{R}] \, F_{\theta}^{a}(\theta,\phi)$$

$$U_{\phi'}^{b}(\theta-\beta, \phi-\alpha)\sin(\theta) \, d\phi \, d\theta \tag{2-31}$$

where β and α are the rotation angles depicted in Figure 2-3,

$$F_{\theta}^{a}(\theta,\phi) = r \, e^{jkr} \, E_{\theta ff}^{a}(\theta,\phi), \text{ and} \tag{2-32}$$

where $U_{\phi'}^{b}$ is a functional of the $H_{\phi'}$-field of Antenna B given by

$$U_{\phi'}^{b}(\theta-\beta, \phi-\alpha) = (r')^2 \int_{0}^{\pi} \int_{-\pi}^{\pi} \left[H_{\phi'}^{b}(r', \tilde{\theta}'-\beta, \tilde{\phi}'-\alpha) \right.$$

$$\left. T_{\theta\theta'}(r', \tilde{\theta}', \tilde{\phi}') \exp[-j\bar{k}(\theta,\phi) \cdot \bar{r}'] \sin(\tilde{\theta}') \right] d\tilde{\phi}' d\tilde{\theta}'. \tag{2-33}$$

18
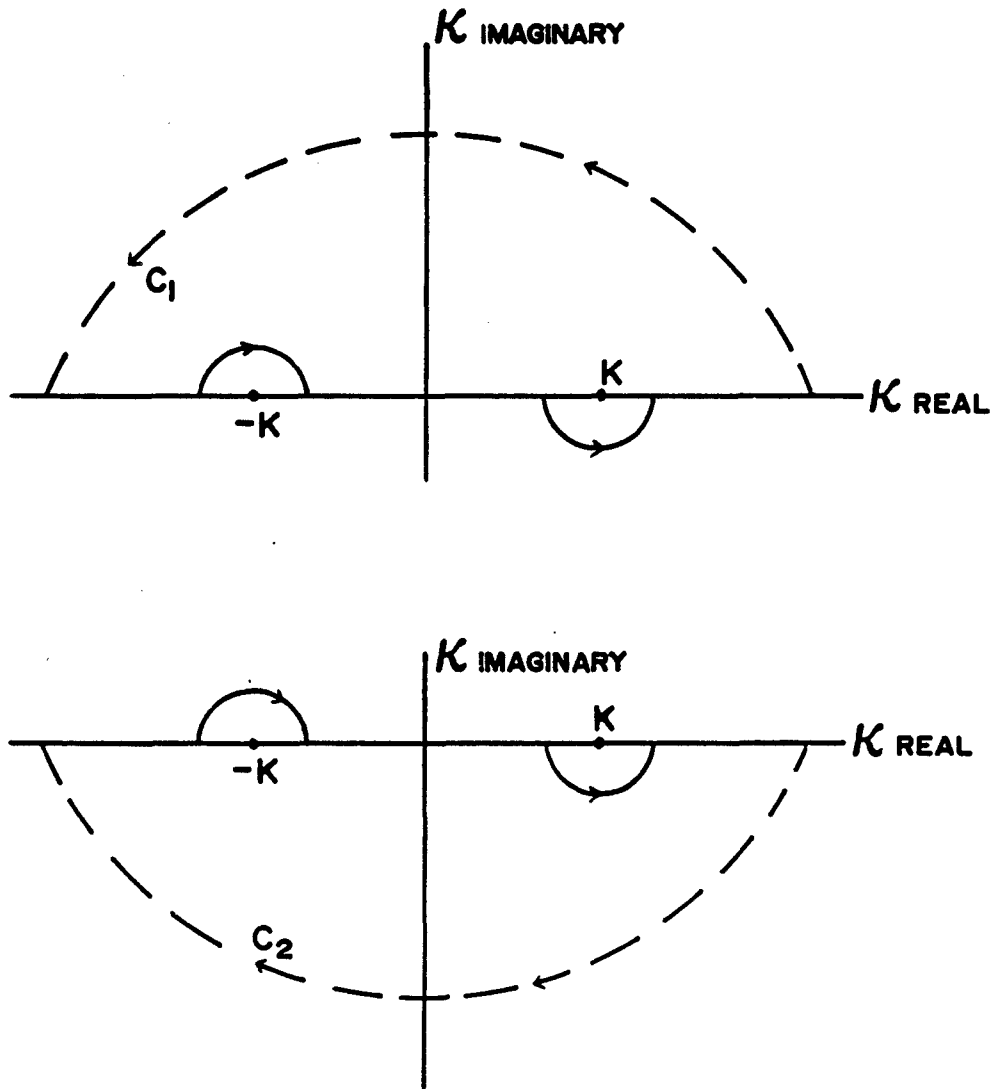
Figure 2-2. Integration contours C_1 and C_2 in the complex κ plane that are used in the spectral representation of the free-space Green's function.
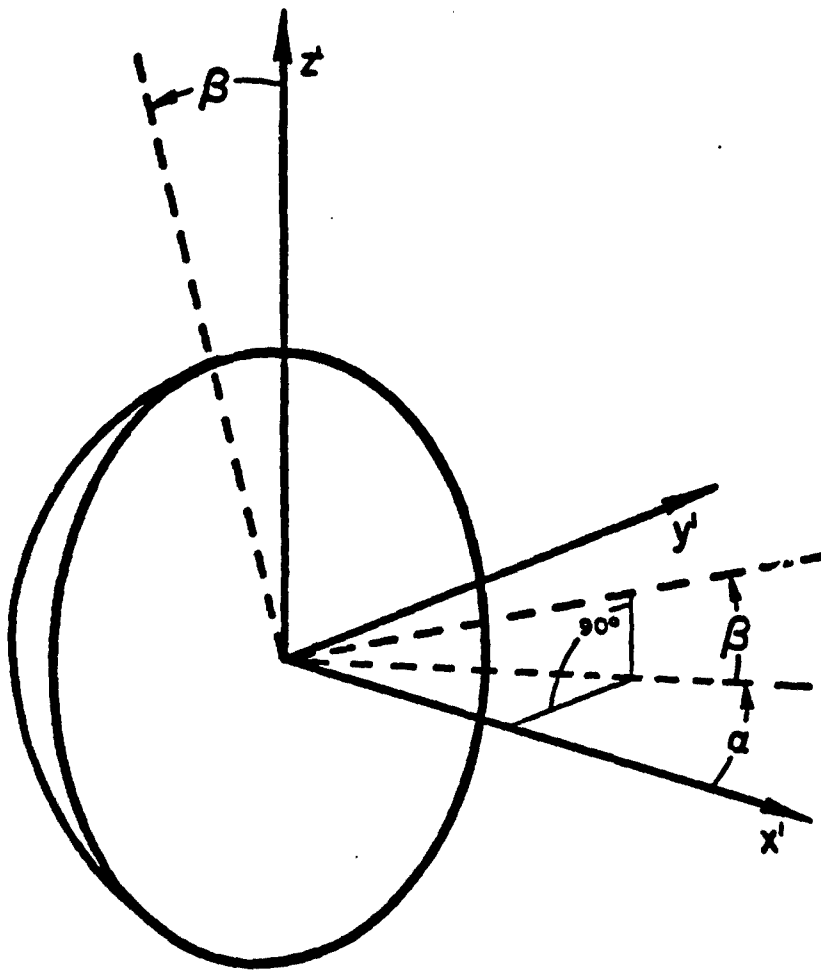
Figure 2-3. Sketch depicting the azimuth rotation angle α and the
elevation rotation angle β associated with Antenna B
of Figure 2-1.

The generalized convolution integrals discussed previously can be utilized along with an approximate relation applicable for $E_r \ll (E_\theta, E_\phi)$,

$$H_\phi = \frac{E_\theta}{Z_o} , \tag{2-34}$$

where Z_o is the impedance of free space, to express (2-33) as $U_{\phi'}^b = U_{\theta'}^b$, where $U_{\theta'}^b$ is

$$U_{\theta'}^b (\theta-\beta, \phi-\alpha) = \frac{k}{Z_o} \int_o^\pi \int_{-\pi}^\pi F_{\theta'}^b (\xi-\beta, \eta-\alpha) \ T_{\theta\theta'}(\theta,\phi|\xi,\eta) \sin\xi \, d\eta \, d\xi . \tag{2-35}$$

The angles (ξ,η) correspond to the usual (θ,ϕ) spherical angles. The functions $F_{\theta'}^b$ and $T_{\theta\theta'}$ are

$$F_{\theta'}^b (\xi-\beta, \eta-\alpha) = re^{jkr} E_{\theta'}^b (\xi-\beta, \eta-\alpha) \quad \text{and} \tag{2-36}$$

$$T_{\theta\theta}(\theta,\phi|\xi,\eta) = (r')^2 \int_o^\pi \int_{-\pi}^\pi \exp[-j[\bar{k}(\theta,\phi)+\bar{k}(\xi,\eta)] \cdot \bar{r}'] T_{\theta\theta'} \, d\tilde{\Omega}' \tag{2-37}$$

respectively, where $d\tilde{\Omega}' = \sin(\tilde{\theta}')d\tilde{\theta}'d\tilde{\phi}'$.

Equation (2-31) can now be written more explicitly as

$$((E_\theta^a \ T_{\theta\theta'}, H_\phi^b)) = \frac{k^2}{Z_o} \int_o^\pi \int_{-\pi}^\pi \exp[-j\bar{k}(\theta,\phi) \cdot \bar{R}] \ F_\theta^a(\theta,\phi) \ \sin(\theta) \times$$

$$\int_o^\pi \int_{-\pi}^\pi F_{\theta'}^b (\xi-\beta, \eta-\alpha) T_{\theta\theta'}(\theta,\phi|\xi,\eta) \sin\xi \ d\eta d\xi \ d\phi d\theta . \tag{2-38}$$

21

This expression for the partial coupling integral has the receiving antenna SAF $F_{\theta'}^b$ convolved with the integral transform $T_{\theta\theta'}$ of the polarization projection function $T_{\theta\theta'}$. Thus, this convolution must be performed for every new rotation angle. However, for our basic computation scenario we wish to rotate the receiving antenna while keeping the transmitting antenna stationary during this set of computations. Accordingly, it would be computationally more efficient to have an expression in which the non-rotating SAF F_{θ}^a of the transmitting antenna rather than $F_{\theta'}^b$ of the receiving antenna was convolved with $T_{\theta\theta'}$. This is readily achieved simply by interchanging the order of integrations in (2-38). The dummy variables (θ, ϕ) and (ξ, η) are also exchanged after the re-ordering of the integrals so that the final integration is expressed in terms of the familiar (θ, ϕ) spherical angles. Thus, the coupling integral becomes

$$((E_{\theta}^a T_{\theta\theta'}, H_{\phi'})) = \frac{k^2}{Z_o} \int_0^\pi \int_{-\pi}^\pi F_{\theta'}^b(\theta-\beta, \phi-\alpha) \sin(\theta) \times$$

$$\int_0^\pi \int_{-\pi}^\pi F_{\theta}^a(\xi,\eta) T_{\theta\theta'}(\theta,\phi|\xi,\eta) \exp[-j\bar{k}(\xi,\eta)\cdot\bar{R}]$$

$$\sin(\xi)\, d\eta d\xi d\phi d\theta . \qquad (2-39)$$

The equivalence of (2-38) and (2-39) is expected since $((E_{\theta}^a T_{\theta\theta'}, H_{\phi}^b))$ is just a multiple convolution. Equation (2-38) is

$$((E_{\theta}^a T_{\theta\theta'}, H_{\phi'}^b)) = (\exp[-j\bar{k}\cdot\bar{R}] F_{\theta}^a) \star F_{\theta'}^b \star T_{\theta\theta'} \qquad (2-40)$$

where the $\star$ here denotes convolution. Similarly, Equation (2-39) is

$$((E_{\theta}^a T_{\theta\theta'}, H_{\phi'}^b)) = F_{\theta}^b \star (\exp[-j\bar{k}\cdot\bar{R}] F_{\theta}^a) \star T_{\theta\theta'} \qquad (2-41)$$

Sufficiency conditions for

$$F_\theta^b \, \ast \, (\exp[-j\bar{k}\cdot\bar{R}]F_\theta^a) \, \ast \, T_{\theta\theta'} \, = \, (\exp[-j\bar{k}\cdot\bar{R}]F_\theta^a) \, \ast \, F_\theta^b \, \ast \, T_{\theta\theta'}$$

$$(2\text{-}42)$$

are the same as given previously in the discussion of the generalized convolution. Less restrictive conditions for the commutability of convolution integrals are given by L. Schwartz in References 20 and 21.

The same procedure is applied to all of the partial coupling integrals except those having E_r^a and H_r^a in their integrand. These integrals are of the order r^{-3} whereas the integrals involving only products of the $(\hat{\theta}, \hat{\phi})$ and $(\hat{\theta}', \hat{\phi}')$ components are of the order r^{-2}. The integrals involving E_r^a and H_r^a are expected to yield a non-negligible contribution to the coupling only if one (or both), of the antennas is (are) electrically very small and the separation distance is about two wavelengths or smaller. The emphasis in this research program is placed on development of efficient algorithms for directive antennas. It appears that the contributions of the radially polarized components will be negligible for realistic situations involving directive antennas and for many situations where one or more of the antennas are electrically small.

The total coupling integral $((\,b,a\,)) = v^{ba}$ is then expressed as the sum of the double convolution integrals for all of the partial couplings involving the $(\hat{\theta}, \hat{\phi})$ components of the transmitting antenna. The expression for v^{ba} is then

$$
\begin{aligned}
v^{ba} = \frac{k^2}{Z_o} \Big[& - F_\theta^b \, \ast \, (\exp[-j\bar{k}\cdot\bar{R}] \, F_\theta^a) \, \ast \, (T_{\theta\theta'} + T_{\phi\phi'}) \\
& + F_\phi^b \, \ast \, (\exp[-j\bar{k}\cdot\bar{R}] \, F_\phi^a) \, \ast \, (T_{\theta\theta'} + T_{\phi\phi'}) \\
& + F_\theta^b \, \ast \, (\exp[-j\bar{k}\cdot\bar{R}] \, F_\phi^a) \, \ast \, (T_{\theta\phi'} + T_{\phi\theta'}) \\
& - F_\phi^b \, \ast \, (\exp[-j\bar{k}\cdot\bar{R}] \, F_\theta^a) \, \ast \, (T_{\theta\phi'} + T_{\phi\theta'}) \Big]
\end{aligned}
$$

$$(2\text{-}43)$$

23

The antenna coupling is more conveniently characterized in terms of the mutual gain M for the antenna pair relative to a pair of isotropic radiators in lieu of the voltage V^{ba}. The mutual gain is defined as

$$M(\bar{R},\beta,\alpha) = \left(\frac{4\pi R}{\lambda}\right)^2 \frac{P_r(\bar{R}, \beta,\alpha)}{P_t} \tag{2-44}$$

where P_r is the received power and P_t is the transmitted power. The mutual gain is expressed in terms of the normalized, dimensionless SAF's $\bar{F}_o^b$ and $\bar{F}_o^a$ that are normalized to unity as

$$M(\bar{R},\beta,\alpha) = \left(\frac{4\pi R}{\lambda}\right)^2 g_b g_a \, k^4 \, \bigg| -F_{o\theta}^b * (exp[-j\bar{k}\cdot\bar{R}]F_{o\theta}^a) * (T_{\theta\theta'} + T_{\phi\phi'})$$

$$+ F_{o\phi}^b * (exp[-j\bar{k}\cdot\bar{R}]F_{o\phi}^a) * (T_{\theta\theta'} + T_{\phi\phi'})$$

$$+ F_{o\theta}^b * (exp[-j\bar{k}\cdot\bar{R}]F_{o\phi}^a) * (T_{\theta\phi'} + T_{\phi\theta'})$$

$$- F_{o\phi}^b * (exp[-j\bar{k}\cdot\bar{R}]F_{o\theta}^a) * (T_{\theta\phi'} + T_{\phi\theta'}) \bigg|^2$$

$$\tag{2-45}$$

where g_b denotes the peak "far-field" gain relative to isotropic gain of Antenna B when used as a receiver for plane wave illumination and g_a denotes the peak far-field gain of Antenna A when used as a transmitter. The mutual gain given by this equation is the quantity of interest in the numerical studies.

D. Obstacle Effects

We consider next two antennas operating in the presence of an obstacle. The obstacle is allowed to have arbitrary but known shape and composition, and it can be located anywhere outside the surfaces enclosing the radiating portions of the two antennas. The derivation of the coupling integrals for two antennas operating in the presence of a single obstacle is outlined in the following paragraphs. The extension to more than one obstacle is then briefly considered.

The situation under study is depicted in Figure 2-4; $\bar{R}$ is again the vector extending from the transmitting Antenna A to the receiving Antenna B. $\bar{R}_a'$ and $\bar{r}$ are vectors extending from Antenna A and the obstacle reference center, respectively, to a field point. $\bar{r}_a$ and $\bar{r}_b$ extend from Antenna A and Antenna B, respectively, to the obstacle reference center. $\bar{r}_1$ traces out the surface of the obstacle.

It is well known that the $\bar{E}$ and $\bar{H}$ fields at a point in the near field can be written as the sum of the incident antenna fields and the obstacle scattered fields,

$$\bar{E}^t = \bar{E}^a + \bar{E}^s, \text{ and} \tag{2-46}$$

$$\bar{H}^t = \bar{H}^a + \bar{H}^s, \tag{2-47}$$

where the superscripts t, a, and s denote total, Antenna A, and scattered, consecutively. The complex voltage V^{bt} induced in Antenna B may be obtained from the coupling integral given in Equation (2-3) by substituting $(\bar{E}^t, \bar{H}^t)$ for $(\bar{E}^a, \bar{H}^a)$ to yield

$$V^{bt} = V^{ba} + V_1^{bs}. \tag{2-48}$$

The voltage V^{ba} is, of course, just the voltage induced in Antenna B by Antenna A in the absence of the scattering obstacles, i.e., the clear-site coupling voltage. The voltage V_1^{bs} is the voltage induced in Antenna B by the scattered fields of the obstacle, and it is given in terms of the coupling integral as

$$V_1^{bs} = -\iint_{S'} [\ \bar{E}^s\ (-\bar{r}_b + \bar{r}') \times \bar{H}^b(\bar{r}') + \bar{H}^s\ (-\bar{r}_b + \bar{r}') \times E^b\ (\bar{r}') \cdot \hat{n}'\ ds'\ ] \tag{2-49}$$

where, as before, S' is an arbitrary surface enclosing Antenna B and $\hat{n}'$ is a unit vector normal to the surface and pointing out of the enclosed volume. Proceeding exactly as in the derivation of the clear-site SAF coupling integrals, the voltage V_1^{bs} is expressed in terms of the

25
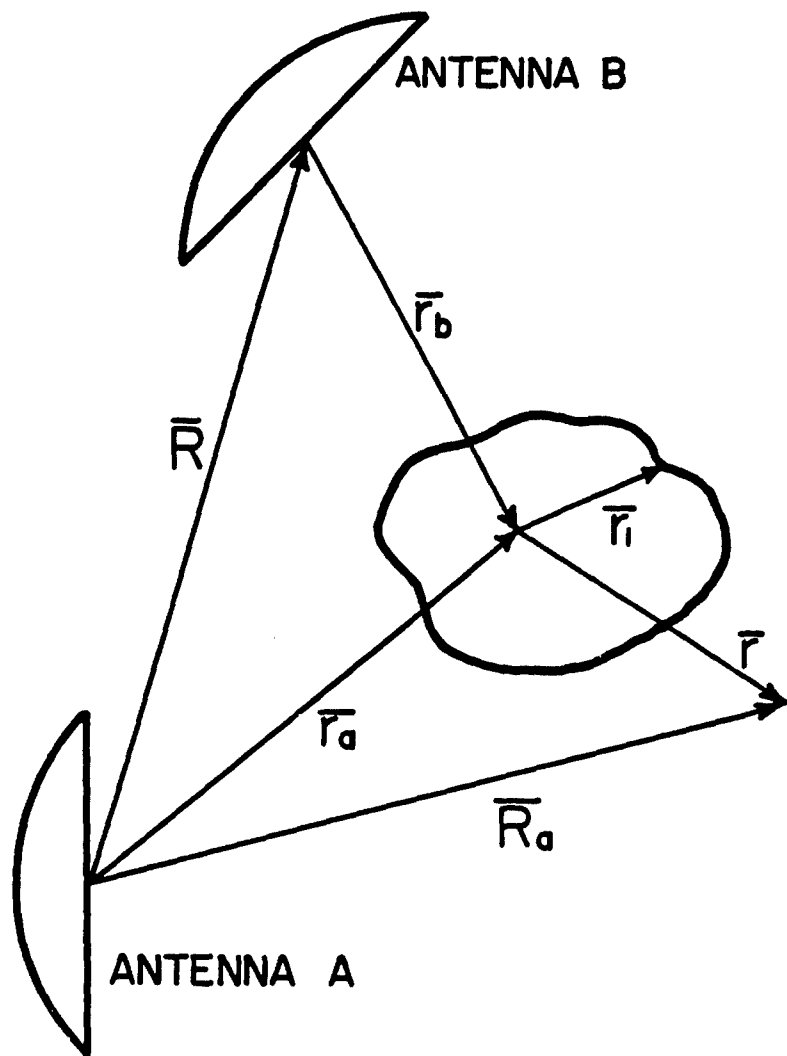
Figure 2-4.   Sketch depicting a scattering obstacle located within
the near-field of two cosited antennas.

far-field quantities $\bar{F}^b(\theta,\phi)$ and $\bar{F}^s_1(\theta,\phi)$ as

$$v^{bs}_1 = \frac{k^2}{Z_o} \Bigg[[- F^b_\theta * (\exp[-j\bar{k}\cdot\bar{R}] F^s_{1\theta}) * (T_{\theta\theta'} + T_{\phi\phi'})$$

$$+ F^b_\phi * (\exp[-j\bar{k}\cdot\bar{R}] F^s_{1\phi}) * (T_{\theta\theta'} + T_{\phi\phi'})$$

$$+ F^b_\theta * (\exp[-j\bar{k}\cdot\bar{R}] F^s_{1\phi}) * (T_{\theta\phi'} + T_{\phi\theta'})$$

$$- F^b_\phi * (\exp[-j\bar{k}\cdot\bar{R}] F^s_{1\theta}) * (T_{\theta\phi'} + T_{\phi\theta'}) \Bigg]_{(2-50)}$$

The SAF $\bar{F}^s_1(\theta,\phi)$ for the scattering obstacle may be obtained with the aid of a slight generalization of the reaction integral for scattering [15]. Let $\bar{\bar{J}}_{1e}(\bar{r}_1)$ and $\bar{\bar{J}}_{1m}(\bar{r}_1)$ denote scattering current dyadics for the electric and magnetic currents induced on the surface of the obstacle when illuminated by an infinitesimal dipole with unit current located at $\bar{r} = (r,\theta,\phi)$. In the limit of very large r, we obtain, via the reaction integral for scattering

$$\bar{E}^s_1(\theta,\phi) = \frac{e^{-jkr}}{r} \iint_S \Bigg[\bar{\bar{J}}_{1e} \cdot (\bar{r}_1) \cdot \bar{E}^a(\bar{r}_a + \bar{r}_1) - \bar{\bar{J}}_{1m}(\bar{r}_1)$$

$$\cdot \bar{H}^a(\bar{r}_a + \bar{r}_1) \Bigg] ds_1 \qquad\qquad (2-51)$$

from whence we can obtain $\bar{F}^s_1(\theta,\phi)$ via the relation $\bar{F}^s_1(\theta,\phi) = r e^{jkr}\bar{E}^s_1(\theta,\phi)$.

An expression for $\bar{F}^s_1(\theta,\phi)$ in terms of far-field pattern variables is desired, and can be obtained by employing the Huygens-Fresnel integral given by Equation (2-24). In particular, the electric field $\bar{E}^a$ of Antenna A becomes

$$\bar{E}^a(\bar{r}_a + \bar{r}_1) = \frac{jk}{2\pi} \iint_{\Omega'} \bar{F}^a(\theta',\phi') \exp\Bigg[-j\bar{k}(\theta',\phi')\cdot(\bar{r}_a+\bar{r}_1) \Bigg] d\Omega' ,$$

$$(2-52)$$

27

and similarly for $\bar{H}^s$. This leads to the following expression for $\bar{F}_1^s(\theta,\phi)$,

$$\bar{F}_1^s(\theta,\phi) = \frac{-jk}{2\pi} \iint_{\Omega'} \bar{F}^a(\theta',\phi') \exp\left[-j\bar{k}(\theta',\phi')\cdot\bar{r}_a\right] \bullet$$

$$\iint_{S_1} \bar{J}_1(\bar{r}_1) \exp\left[-j\bar{k}(\theta',\phi')\cdot\bar{r}\right] ds_1 d\Omega' \tag{2-53}$$

where $\bar{J}_1 = \bar{J}_{1e} + \bar{J}_{1m}$ and where $d\Omega' = \sin(\theta') d\theta' d\phi'$. This can be cast into a more familiar form by defining the obstacle scattering dyadic $\bar{\bar{S}}_1(\theta,\phi \mid \theta',\phi')$,

$$\bar{\bar{S}}_1(\theta,\phi \mid \theta',\phi') = j\omega\mu \iint_{S_1} \bar{J}_1(\bar{r}_1 \mid \theta,\phi) \exp\left[-j\bar{k}(\theta',\phi')\cdot \bar{r}_1\right] ds_1 . \tag{2-54}$$

The resulting expression for $F_1^s(\theta,\phi)$ is then

$$\bar{F}_1^s(\theta,\phi) = \frac{k}{2\pi\omega\mu} \iint \bar{\bar{S}}_1(\theta,\phi \mid \theta',\phi') \cdot \bar{F}^a(\theta',\phi') \exp\left[-j\bar{k}(\theta',\phi) \cdot \bar{r}_a\right] d\Omega' \tag{2-55}$$

This equation, as well as Equations (2-51) through (2-54) were derived with respect to polarization components that are convenient for the description of the surface currents on the obstacle. However, Equation (2-55) is valid for any choice of polarization convention. Accordingly, spherical $(\hat{\theta},\hat{\phi})$ components are now chosen in order for $\bar{F}_1^s(\theta,\phi)$ to blend with the "clear-site" SAF equations.

The foregoing analysis is readily extended to multiple obstacles if the multiple obstacle scattering dyadic $\bar{\bar{S}}$ can be specified from theory or experiment. $\bar{\bar{S}}$ can be approximated as the sum of the isolated single obstacle scattering dyadics if the effects of multiple scattering can be ignored. Perturbation techniques for small metal cylinders or spheres exist for improving the results obtained from the superposition of isolated obstacle scattered fields [22,23].

28

SECTION III
APPROXIMATE SAF ANALYSIS

A. Introduction

The rigorous theory and equations presented in Section II have the very desirable attribute of being applicable to antennas and/or scatterers of low, moderate, or high directivity. Additionally, they are valid for any orientations/arrangements of the antenna and scattering objects. Accordingly, the rigorous SAF equations appear to be well suited for analyzing antenna coupling under both clear-site and obstructed conditions for situations where there are questions concerning the PWS computations. However, one can anticipate that the computer core storage and execution times for electrically large antennas/sc. terers may become prohibitively large for a computer program based on the rigorous SAF analysis.

The rigorous SAF antenna coupling analysis requires the evaluation of complex integral transforms of $(T_{\theta\theta}$, $T_{\phi\phi}$, etc.) of the polarization transformation operators $(T_{\theta\theta}$, $T_{\phi\phi}$, etc.) and the evaluation of a pair of nested convolution integrals. The integral transform is a four-dimensional complex function of angular variables while each of the convolution integrals are two-dimensional complex functions of angular variables. Assuming that the functions are sampled at the Nyquist rate over, say, a hemisphere, it can readily be deduced that computer storage and execution times can become excessive for closely-spaced electrically-large antennas. Indeed, storage requirements and execution times are significant problem areas even for the inherently fast PWS-based algorithms that employ FFT processing [10,11]. Accordingly, it is recognized forthwith that some simplifications must be made in order to obtain a practical and versatile SAF algorithm that can be applied to a large class of antenna coupling situations.

Analytical and numerical studies were initiated during this reporting period to improve the efficiency of the computer programs employing SAF equations without seriously degrading accuracy. The stationary phase evaluation of radiation integrals has been applied along with sampling theory to furnish guidelines for choosing the required angular integration regions for the convolution integrals and the integral transforms. The

29

stationary phase analysis was also employed in the development of series representation of the integral transforms $T_{\theta\theta}$, $T_{\phi\phi}$, etc. Numerical studies were begun to study the impact of integration region and sample spacing on the accuracy of the antenna coupling computations. The analysis and preliminary numerical data are presented and discussed in the following paragraphs.

B   Stationary Phase Evaluation

1.   Integration Region

The integral transforms such as $T_{\theta\theta}$ given in Equation (2-37) and the convolution integrals such as $((E_\theta^a \, T_{\theta\theta}, \, H_\phi,))$ given in Equation (2-39) are of the general form,

$$I(\gamma_1, \gamma_2) = \iint A(\gamma_1', \gamma_2') \, \exp\left[-j(kr) \, f \, (\gamma_1, \gamma_2 | \gamma_1', \, \gamma_2') \right] \, d\gamma_1' d\gamma_2' \,. \tag{3-1}$$

P. Debeye [24] has devised a method for evaluating this type of integral, known as the method of stationary phase, or the method of steepest descent. The method is based on the observation that, for kr >>1, the major contribution from the integrand comes from the region in (γ_1', γ_2') space where the phase function (kr) $f(\gamma_1, \gamma_2 | \gamma_1', \gamma_2')$ is slowly varying compared to the largest significant variation of the function $A(\gamma_1', \gamma_2')$. This region of relatively slow phase variation is centered at the point where the first derivative of the phase function vanishes, known as the stationary phase point. The region of comparatively slow phase variation is frequently referred to as the stationary phase region.

The integrand rapidly becomes increasingly oscillatory when the integration extends outside the stationary phase region. The contribution of this exterior region is typically very small compared to the contribution from the stationary phase region, provided the maximum of a sharply peaked $A(\gamma_1', \gamma_2')$ is located well within the stationary phase region or provided that the parameter kr is sufficiently large.

In order to find the stationary phase point, the phase function kr $f(\gamma_1, \gamma_2 | \gamma_1', \gamma_2')$ is expanded to second order in a Taylor series in two variables about the points γ_{10}' and γ_{20}',

30

$$kr \cdot f(\gamma_1, \gamma_2 | \gamma_{10}' + h, \gamma_{20}' + g) = kr \cdot f(\gamma_{10}', \gamma_{20}') +$$

$$\left[h \frac{\partial}{\partial \gamma_1'} + g \frac{\partial}{\partial \gamma_2'} \right] (kr) \, f(\gamma_1, \gamma_2 | \gamma_1', \gamma_2') \Big|_{\gamma_{10}', \, \gamma_{20}'}$$

$$+ \frac{1}{2} \left[h \frac{\partial}{\partial \gamma_1'} + g \frac{\partial}{\partial \gamma_2'} \right]^2 f \, (kr) \, f(\gamma_1, \gamma_2 | \gamma_1', \gamma_2') \Big|_{\gamma_{10}', \, \gamma_{20}'},$$

$$\tag{3-2}$$

and the stationary phase point is found from the requirement that

$$\left[h \frac{\partial}{\partial \gamma_1'} \cdot g \frac{\partial}{\partial \gamma_2'} \right] k_0 r \, f(\gamma_1, \gamma_2 | \gamma_1', \gamma_2') \Big|_{\gamma_{10}', \, \gamma_{20}'} = 0. \tag{3-3}$$

The phase functions to be evaluated in the SAF integrals can be written in the form

$$(kr) \, f(\gamma_1, \gamma_2 | \gamma_1', \gamma_2') = (kr) \, \{ \sin(\gamma_1)\cos(\gamma_2)\sin(\gamma_1')\cos(\gamma_2')$$

$$+ \sin(\gamma_1)\sin(\gamma_2)\sin(\gamma_1')\sin(\gamma_2')$$

$$+ \cos(\gamma_1)\cos(\gamma_1') \, \}. \tag{3-4}$$

Expanding the phase function in its Taylor series expansion and applying the condition (3-3) leads to the sensible result that the stationary phase point is located at $\gamma_1' = \gamma_1$ and $\gamma_2' = \gamma_2$.

The extent of the stationary phase region can be estimated as follows [11]. First, a coordinate rotation is effected to align the z-axis of a spherical coordinate system along the stationary phase direction (γ_1, γ_2). The phase function in this new coordinate system is then

$$(kr) \, f(\Theta) = kr \, \cos(\Theta) \tag{3-5}$$

where Θ is the polar angle that opens from the new z-axis. Next, the criterion is adopted that the edge of the stationary phase region occurs at the angular location where the rate of change of the phase function is equal to twice the most rapid variation of the function A. Thus, we need

31

to equate the first derivative of the phase function with respect to the angular integration variables to twice the highest-frequency Fourier component of A. For (non-supergain) antenna pattern functions and/or obstacle scattering functions, two times the highest-frequency Fourier component of $A(\Theta)$ is bounded by $\pi D/\lambda$, where D is either (1) the diameter of the sphere circumscribing the radiating portion of the antenna or scatterer or (2) two wavelengths, whichever is larger. For coupling integrals, for which $A(\Theta)$ is essentially a product of two non-supergain antenna-like pattern functions, twice the highest-frequency component can be taken as $\pi(D_a + D_b)/\lambda$ where D_a and D_b are (1) either the diameter of spheres circumscribing the radiating portions of Antenna A and Antenna B, respectively or (2) two wavelengths each, whichever is larger. Thus, for coupling integrals we have

$$(k_o r)\, \sin(\Theta_p) = \pi\, \frac{(D_a + D_b)}{\lambda}, \qquad (3-6)$$

where Θ_p denotes the "edge" of the stationary phase region. This leads to the result [11],

$$\sin(\Theta_p) = \frac{(D_a + D_b)}{2r}. \qquad (3-7)$$

The sample spacing can be chosen by invoking the Nyquist criterion. Accordingly, the angular increments should not be larger than

$$\Delta\gamma = \frac{1}{\dfrac{\pi(D_a + D_b)}{\lambda}} \qquad (3-8)$$

in order to satisfy the Nyquist sampling rate.

The integration region and sample spacing given by Equations (3-7) and (3-8), respectively, provide guidelines for numerical computations. Larger integration regions and/or finer sample spacings may be required in some applications in order to achieve a specified level of accuracy. On the other hand, some relaxation of these criteria may be permissible for some EMC applications The numerical studies that are in progress on this

32

contract should provide additional insight into the impact of the
integration region and sampling rate for EMC applications.

2. Approximation for the Integral Transforms

An approximation is sought for the angular space representation,
i.e., the integral transforms $T_{\theta\theta'}$, $T_{\phi\phi'}$, etc., of the polarization
transformation operator. It will suffice to consider only the integral for
$T_{\theta\theta'}$ since the same procedure is applicable to all of the T's. The integral
for $T_{\theta\theta}$ is given by Equation (2-37) as

$$T_{\theta\theta}(\theta,\phi|\xi,\eta) = (r')^2 \int_0^\pi \int_{-\pi}^\pi \exp[-j\ \overline{K}(\theta,\phi) + [\overline{K}(\xi,\eta)] \cdot \overline{r}'] \ T_{\theta\theta'} \sin(\tilde{\theta}')d\tilde{\phi}'d\tilde{\theta}', \tag{3-9}$$

where $T_{\theta\theta'}$ is given in Table 2-1 as

$$T_{\theta\theta'} = \cos(\tilde{\theta})\cos(\tilde{\phi})\cos(\tilde{\theta}')\cos(\tilde{\phi}') + \cos(\tilde{\theta})\sin(\tilde{\phi})\cos(\tilde{\theta}')\sin(\tilde{\phi}')$$

$$+ \sin(\tilde{\theta})\sin(\tilde{\theta}') \quad . \tag{3-10}$$

The integrations in Equation (3-9) are performed over the surface of a
sphere circumscribing Antenna B. Axonometric plots of $T_{\theta\theta'}$ and $T_{\phi\phi'}$ are
shown in Figures 3-1 and 3-2, respectively, for a circumscribing sphere of
radius 5λ , where λ is the wavelength. These plots display the functional
form of $T_{\theta\theta'}$ and $T_{\phi\phi'}$ versus elevation angle $\tilde{\theta}'$ and azimuth angle $\tilde{\phi}'$.

In order to develop a conventional asymptotic series representation
for $T_{\theta\theta'}$, it is necessary to expand the exact polarization transformation
operator $T_{\theta\theta'}$ in a two-dimensional Taylor series about the stationary phase
point of the phase function $[\overline{K}(\xi,\eta) + \overline{K}(\theta,\phi)] \cdot \overline{r}(\tilde{\theta}',\tilde{\phi}')$. The exact phase
function is also replaced by its two-dimensional Taylor series expansion to
second order about the stationary phase point, which occurs along the
direction of the resultant wavevector $\overline{K} = \overline{K}(\xi,\eta) + \overline{K}(\theta,\phi)$. This leads to
an approximation for $T_{\theta\theta'}$ of the form

$$T_{\theta\theta'}(\xi,\eta|\theta,\phi) = \exp\{ -jk\tilde{r}' \ [U_x\tilde{U}'_{xo} + U_y\tilde{U}'_{yo} + U_z\tilde{U}'_{zo}] \ \}$$

$$(r')\sum_m \sum_n a_{mn} \int_{-\infty}^\infty \int_{-\infty}^\infty (\tilde{\theta}-\tilde{\theta}'_0)^m (\tilde{\phi}'-\tilde{\phi}_0)^n \exp\left\{ (\frac{jkr'}{2}) \right.$$

$$\left. [b_1(\tilde{\theta}'-\tilde{\theta}'_0)^2 + b_2(\tilde{\phi}'-\tilde{\phi}'_0)^2] \right\} d\tilde{\theta}'d\tilde{\phi}'$$
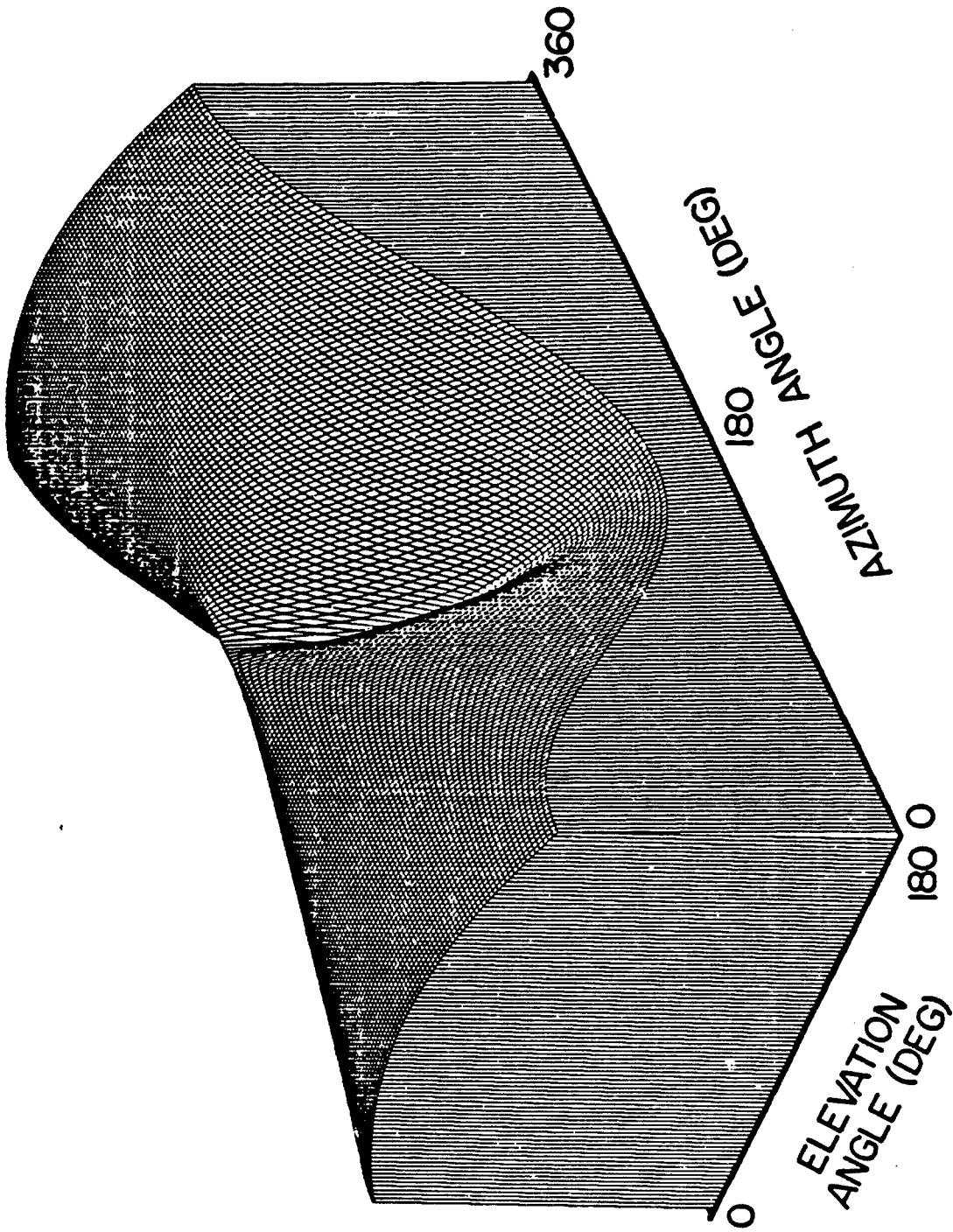
Figure 3-1. Axonometric plot of the polarization transformation function $T_{\theta\theta}$, for a sphere of radius equal to 5 wavelengths.
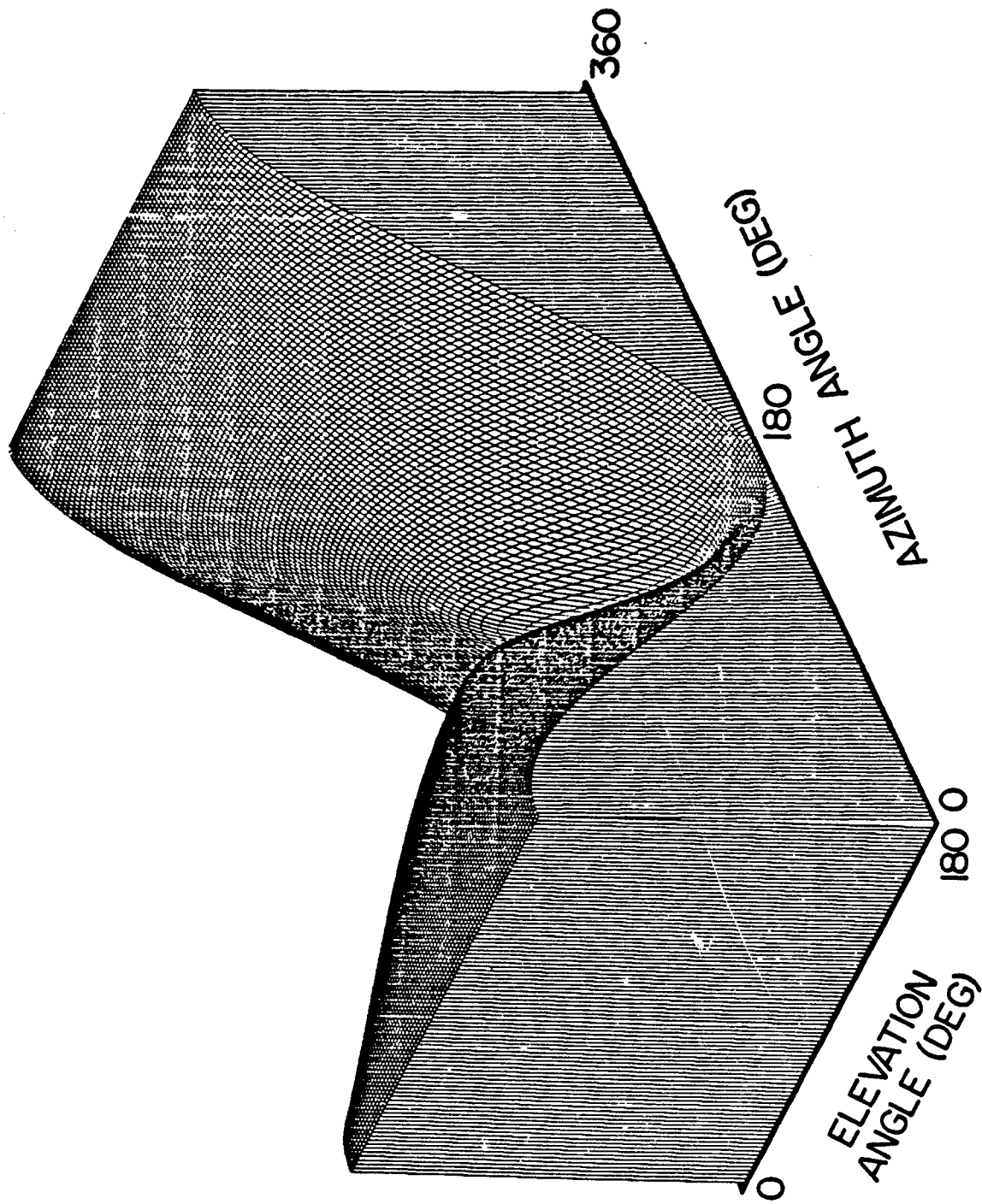
Figure 3-2. Axonometric plot of the polarization transformation function $T_{\phi\phi'}$ for a sphere of radius equal to 5 wavelengths.

ELEVATION ANGLE (DEG)

AZIMUTH ANGLE (DEG)

360

180

180   0

0

35

where a_{mn} are the coefficients of the power series expansion for $T_{\theta\theta}'$
$\sin(\tilde{\theta}')$ and where b_1 and b_2 are computed as

$$b_1 = \frac{\partial^2}{\partial\tilde{\theta}'^2} [U_x \tilde{U}_x' + U_y \tilde{U}_y' + U_z \tilde{U}_z'] \Big|_{\tilde{\theta}_o', \tilde{\phi}_o'} \text{, and} \qquad (3\text{-}12)$$

$$b_2 = \frac{\partial^2}{\partial\tilde{\phi}'^2} [U_x \tilde{U}_x' + U_y \tilde{U}_y' + U_z \tilde{U}_z'] \Big|_{\tilde{\theta}_o', \tilde{\phi}_o'} \text{.} \qquad (3\text{-}13)$$

The variables U_x, U_y, U_z, are

$$U_x = \sin(\xi)\cos(\eta) + \sin(\theta)\cos(\phi), \qquad (3\text{-}15)$$

$$U_y = \sin(\xi)\sin(\eta) + \sin(\theta)\sin(\phi), \text{ and} \qquad (3\text{-}16)$$

$$U_z = \cos(\xi) + \cos(\theta) \text{.} \qquad (3\text{-}17)$$

Similarly, the $\tilde{U}_x'$, $\tilde{U}_y'$ and $\tilde{U}_z'$ are

$$\tilde{U}_x' = \sin(\tilde{\theta}')\cos(\tilde{\phi}'), \qquad (3\text{-}18)$$

$$\tilde{U}_y' = \sin(\tilde{\theta}')\sin(\tilde{\phi}'), \text{ and} \qquad (3\text{-}19)$$

$$\tilde{U}_z' = \cos(\tilde{\theta}') \text{.} \qquad (3\text{-}20)$$

The variables $\tilde{U}_{xo}'$, $\tilde{U}_{yo}'$ and $\tilde{U}_{zo}'$ are obtained from these last three equations
by evaluating them at the stationary phase point $(\tilde{\theta}_o', \tilde{\phi}_o')$.

The integral appearing in Equation (3-11) is of a well known Gaussian
form. Closed-form expressions can be obtained for the various terms in the
series. However, there are important drawbacks to this approximation. In
particular, the second-order expansion for the phase term is accurate only
over a very small portion of the stationary phase region unless kr' is
extremely large. Many additional terms would be needed in the power series
expansion of the phase function in order to obtain an accurate approximation
for the phase function over the stationary phase region for moderate or
small values of kr. The integral would then have to be computed
numerically, which would make the approximation impractical to use.

36

Moreover, this type of asymptotic series for $T_{\theta\theta}'$ may not converge if too many terms are used in the expansion for $T_{\theta\theta}' \sin(\tilde{\theta}')$, and hence one must determine the optimum number of terms to use [25].

The shortcomings of the conventional asymptotic expansion in the $(\tilde{\theta}',\tilde{\phi})$ variables can be circumvented by evaluating $T_{\theta\theta}'$ in terms of the $(\tilde{U}_x',\tilde{U}_y',\tilde{U}_z')$ variables. Equation (3-9) is thus rewritten as

$$T_{\theta\theta}' = (r')^2 \int_0^\pi \int_{-\pi}^\pi \exp\{-jkr'[\,U_x\tilde{U}_x' + U_y\tilde{U}_y' + U_z\tilde{U}_z'\,]\} T_{\theta\theta}'(\tilde{U}_x',\tilde{U}_z')d\Omega' \ , \tag{3-21}$$

where

$$d\,\widehat{\Omega}' = \sin(\tilde{\theta}')d\tilde{\theta}'d\tilde{\phi}' \ . \tag{3-22}$$

The exact polarization transform operator $T_{\theta\theta}'$ can be written in terms of $(\tilde{U}_x',\tilde{U}_z')$ as

$$T_{\theta\theta}' = [\,bA(\tilde{U}_x',\tilde{U}_z')\,\tilde{U}_z'^2 + B(\tilde{U}_x',\tilde{U}_z')\,] \ , \tag{3-23}$$

where the functions $A(\tilde{U}_x',\tilde{U}_z')$ and $B(\tilde{U}_x',\tilde{U}_z')$ are

$$A(\tilde{U}_x',\tilde{U}_z') = [(1+a\,\tilde{U}_x')^2 - b\,\tilde{U}_z'^2(1+a\,\tilde{U}_x)]^{\frac{1}{2}}[\,1-\tilde{U}_z'^2]^{\frac{1}{2}}, \text{ and} \tag{3-24}$$

$$B(\tilde{U}_x',\tilde{U}_z') = [\,1+a\,\tilde{U}_x' - b\,\tilde{U}_z'^2]^{\frac{1}{2}}\,[1+a\,\tilde{U}_x']^{-\frac{1}{2}}\,[1-\tilde{U}_z'^2]^{\frac{1}{2}} \ . \tag{3-25}$$

The parameters b and a are

$$b = \frac{r'^2}{R^2+r'^2} \quad , \text{ and} \tag{3-26}$$

$$a = \frac{2Rr'}{R^2+r'^2} \ . \tag{3-27}$$

The functions $A(\tilde{U}_x',\tilde{U}_z')$ and $B(\tilde{U}_x',\tilde{U}_z')$ are expanded in a two-dimensional Taylor series expansion about the stationary phase point $(\tilde{U}_{xo}',\tilde{U}_{zo}')$ to yield

37

a power series expansion for $T_{\theta\theta'}$,

$$T_{\theta\theta'} = \sum_m \sum_n C_{mn} (\tilde{U}'_x - \tilde{U}'_{xo})^m (\tilde{U}'_z - \tilde{U}'_{zo})^n . \qquad (3\text{-}28)$$

Thus, it is seen from Equations (3-28) and (3-21) that it is necessary to evaluate integrals of the type

$$I_{mn} = \int_0^\pi \int_{-\pi}^\pi U_x'^m U_z'^n \exp \{-jkr' [U_x\tilde{U}'_x + U_y\tilde{U}'_y + U_z\tilde{U}'_z]\} \, d\Omega' \qquad (3\text{-}29)$$

It may readily be discerned that the integral I_{mn} can be obtained from the integral I_{oo} for m and n both equal to zero. In particular, the integral I_{mn} is obtained from I_{oo} by differentiating with respect to U_x and U_z, to wit:

$$I_{mn} = \frac{1}{[-jkr]^{(m+n)}} \left[\frac{\partial^m}{\partial U_x}\right] \left[\frac{\partial^n}{\partial U_z^n}\right] I_{oo} . \qquad (3\text{-}30)$$

Next, we note that the integral I_{oo} obtained from Equation (3-29) by setting m=n=0 can, after a coordinate rotation designed to align the polar axis in the stationary phase direction along the resultant wavevector, be integrated to yield

$$I_{oo}(U_x, U_y, U_z) = (4\pi) \frac{\sin[k_o r'U]}{k_o r'U} \qquad (3\text{-}31)$$

where

$$U = [U_x^2 + U_y^2 + U_z^2]^{\frac{1}{2}} \qquad (3\text{-}32)$$

and where (U_x, U_y, U_z) are as previously defined by Equations (3-15), (3-16), and (3-17). I_{oo} is readily differentiated any number of times with respect to U_x, U_y or U_z. The derivatives of all order are continuous and bounded.

The general properties of the $(\tilde{U}'_x, \tilde{U}'_z)$ series expansion for $T_{\theta\theta'}$ are still under study. However, preliminary results of the analysis indicate that the series converges for all r' < R, a condition that is always fulfilled for antennas whose circumscribing spheres do not touch one another. The preliminary results also strongly indicate that this series converges much faster than the conventional asymptotic series, and

38

consequently, fewer terms are needed to achieve a specified acccuracy. Work has been performed to evaluate the C_{mn} coefficients for the T Taylor series and to obtain the analytical expressions for the integrated I_{mn} terms out to fourth order in U_x' and to second order in U_z'. However, the current version of GTSAF employs only the leading integrated term I_{oo}. This simplification permits considerable reduction in computer run time while maintaining good accuracy.

SECTION IV

NUMERICAL RESULTS

A. Introduction

In this section, numerical data are presented and discussed to illustrate the general capabilities of the SAF-based antenna coupling algorithm and two related auxiliary algorithms. Firstly, coupling data were computed via the computer program SSAF for a pair of $\frac{1}{2}-\lambda$ dipoles and for a pair of $10-\lambda$ circular aperture antennas. This simplified version of the full SAF computer program GTSAF employs function statements to generate the spherical angular functions for the antennas under study. Also, the full expression for the integral transform $T_{\theta\theta}$ ' and $T_{\phi\phi}$ ' of the polarization projection operator is approximated by the leading term I_{oo}, given by Equation (3-31), whose 3-dB beamwidth has been adjusted to more closely replicate the mainbeam of the exact $(T_{\theta\theta}' + T_{\phi\phi}')$. Secondly, mutual coupling data is calculated via GTSAF for a pair of directive antennas for clear site as well as blocked conditions in the near-field, and compared with experimental data. Thirdly, the auxiliary programs GTOBS and EHPARAB, for computing composite antenna/obstacle SAF's and for generating paraboidal reflector antenna SAF's, respectively, are briefly discussed.

B. General Trends

SSAF was used primarily to study general trends in the mutual gain curves and to study the sensitivity of the mutual gain curves to the size of the integration region used in the computations. The key results for the geometry depicted in Figure 4-1 can be summarized with the aid of coupled power curves for a pair of $\frac{1}{2}-\lambda$ dipoles and for a pair of $10-\lambda$ uniformly-illuminated circular aperture antennas. The coupled power curves were computed versus the elevation rotation angle for a fixed skew angle ξ_o for the geometry shown in Figure 4-1. It should be noted that the coupled power curves obtained for this geometry are equivalent to the curves that would be obtained when $\xi_o = 0^o$ with receiving Antenna B located at the longitudal distance $X = R \cos(\xi_o)$ and vertical separation $Z = R \sin(\xi_o)$ and where the rotation angles β and β', respectively, for the two situations are related as $\beta = \beta'-\xi_o$.

40
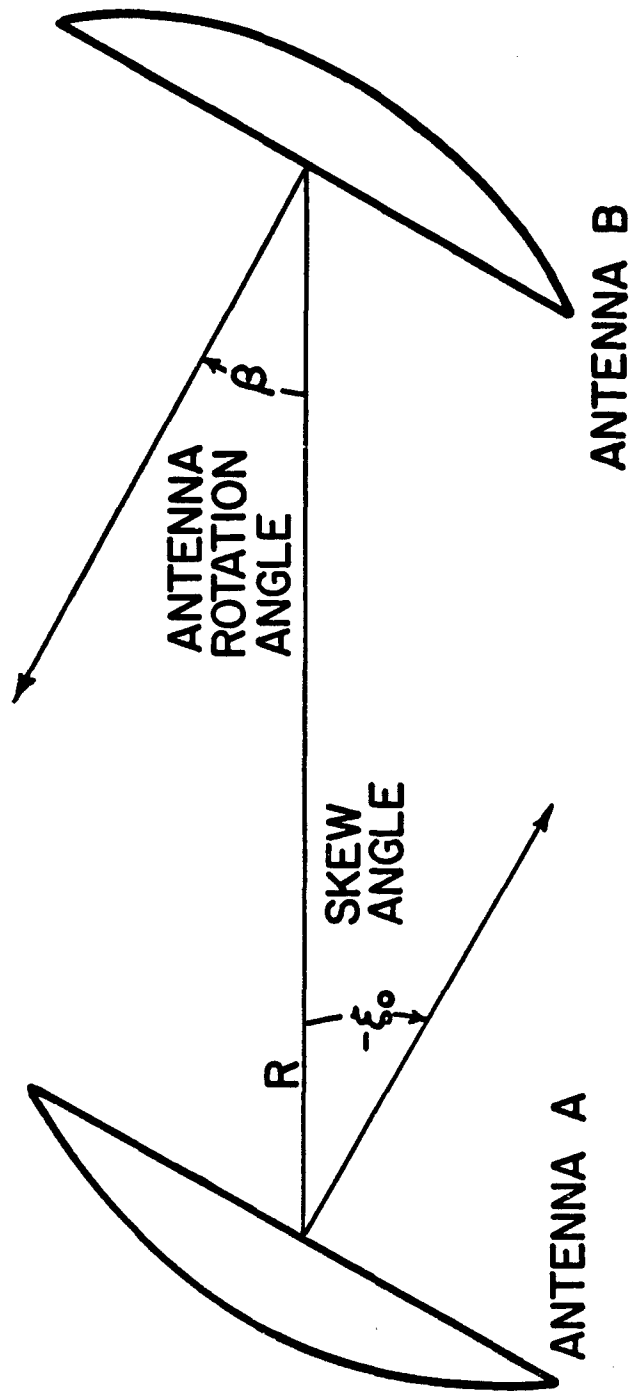
Figure 4-1. Sketch depicting the geometry employed for the computation of relative power coupled to Antenna B from Antenna A.

The integration integral was always chosen to extend only over the mainbeam of the function ($T_{\theta\theta'} + T_{\phi\phi'}$). The integration range of the outermost convolution integral was varied in the numerical tests. Good agreement was achieved between the near-field electric fields computed from SSAF with one antenna replaced by an infinitesimal dipole and the near-field electric fields computed from aperture integration [4] when Equation (2-38) was integrated in the aforementioned manner. The agreement was less satisfactory when Equation (2-38) was integrated in this approximate fashion. Accordingly, the SSAF computations contained herein were based on Equation (2-38) with the roles of Antenna A and Antenna B reversed. Since the antennas are both identical and reciprocal, the coupling data computed in this manner is equivalent to the coupling data obtained for the situation depicted in Figure 3-3 where Antenna A is fixed at the skew angle $-\xi_0$ and Antenna B is rotated through angle β. The data and discussions in the following paragraphs are presented in terms of this latter situation just described.

The coupled power curves computed from SSAF for a pair of $\frac{1}{2}-\lambda$ dipoles separated by 1λ are compared with the coupled power curves computed from the Ohio State Piecewise Sinusoidal (OHSPS) wire program in Figures 4-2 and 4-3. The curve shown in Figure 4-2 was computed for a pair of non-skewed dipoles, while the curve shown in Figure 4-3 was computed for a skew angle of $\xi_0 = -90°$. The integration range for both curves was the entire front hemisphere defined by ($0° \le \theta \le 180°$, $-180° \le \phi \le 180°$). Good agreement is achieved between the SSAF and the OHSPS data for the non-skewed arrangement. The relatively poor agreement for $\xi_0 = -90$ degrees may indicate that the radially polarized field cannot be ignored for this arrangement.

The plots of coupled power shown in Figures 4-4 through 4-12 for two $10-\lambda$ aperture antennas provide useful and interesting information concerning general trends and the impact of the integration range on computational accuracy. The figures are sequenced according to increasing separation distances of 10λ, 25λ, and 40λ, which are equal to 0.05, 0.125, and 0.2, consecutively, of the far-field distance of each aperture antenna. The transmitting Antenna A was skewed at $\xi_0 = -26°$ for all of the computations presented by these figures. Three curves are shown for each

42
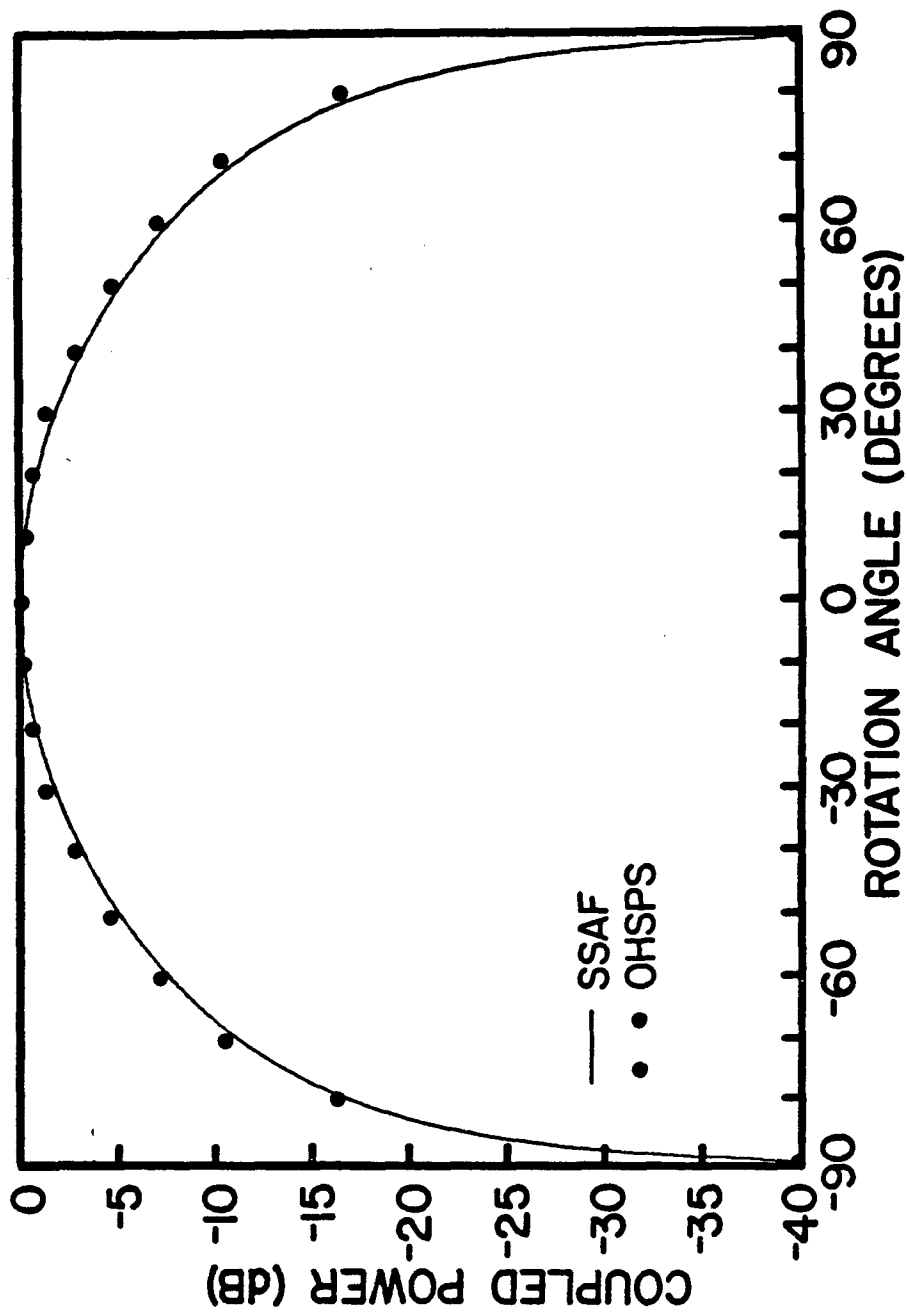
Figure 4-2. Coupled power versus rotation angle for a pair of 1/2-λ dipole antennas for a separation distance of 1λ for a skew angle of zero degrees for integration over the forward hemisphere.

43
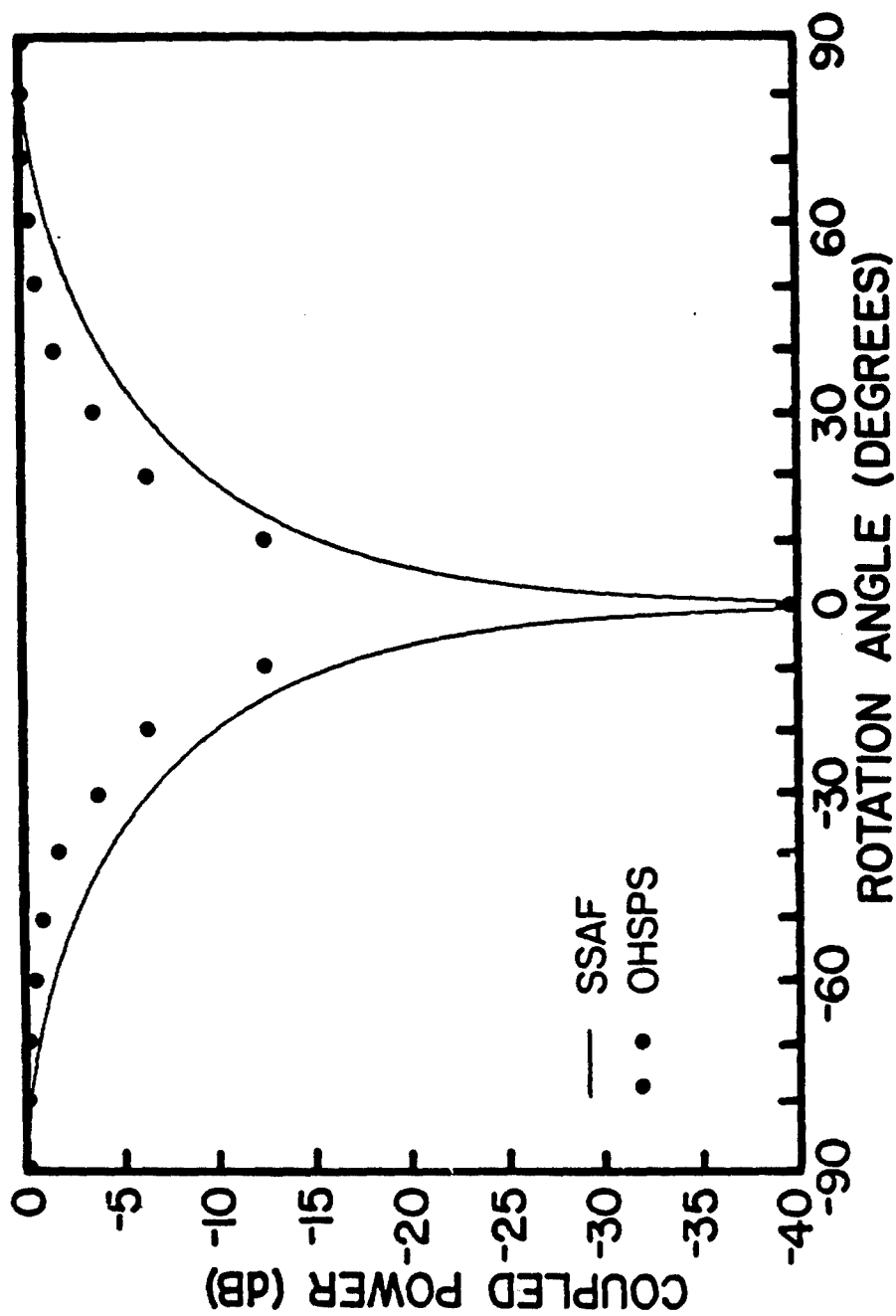
Figure 4-3. Coupled power versus rotation angle for a pair of 1/2-λ dipole antennas for a separation distance of 1λ for a skew angle of -90.0 degrees for integration over the forward hemisphere.

44
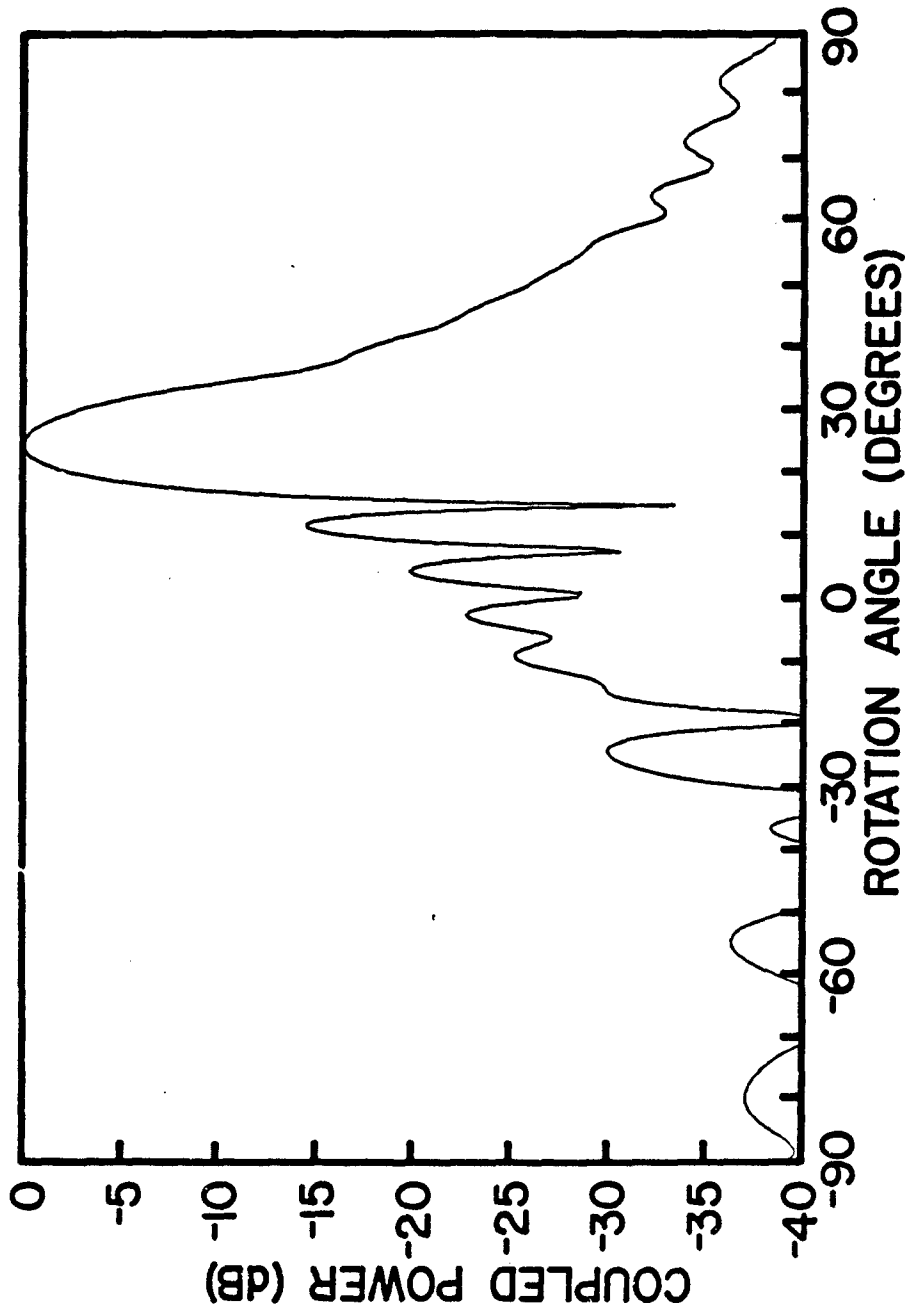
Figure 4-4. Coupled power versus rotation angle for a pair of 10-λ circular aperture antennas for a separation distance of 10λ for a skew angle of −26.0 degrees for integration over an integration range of 70 degrees.
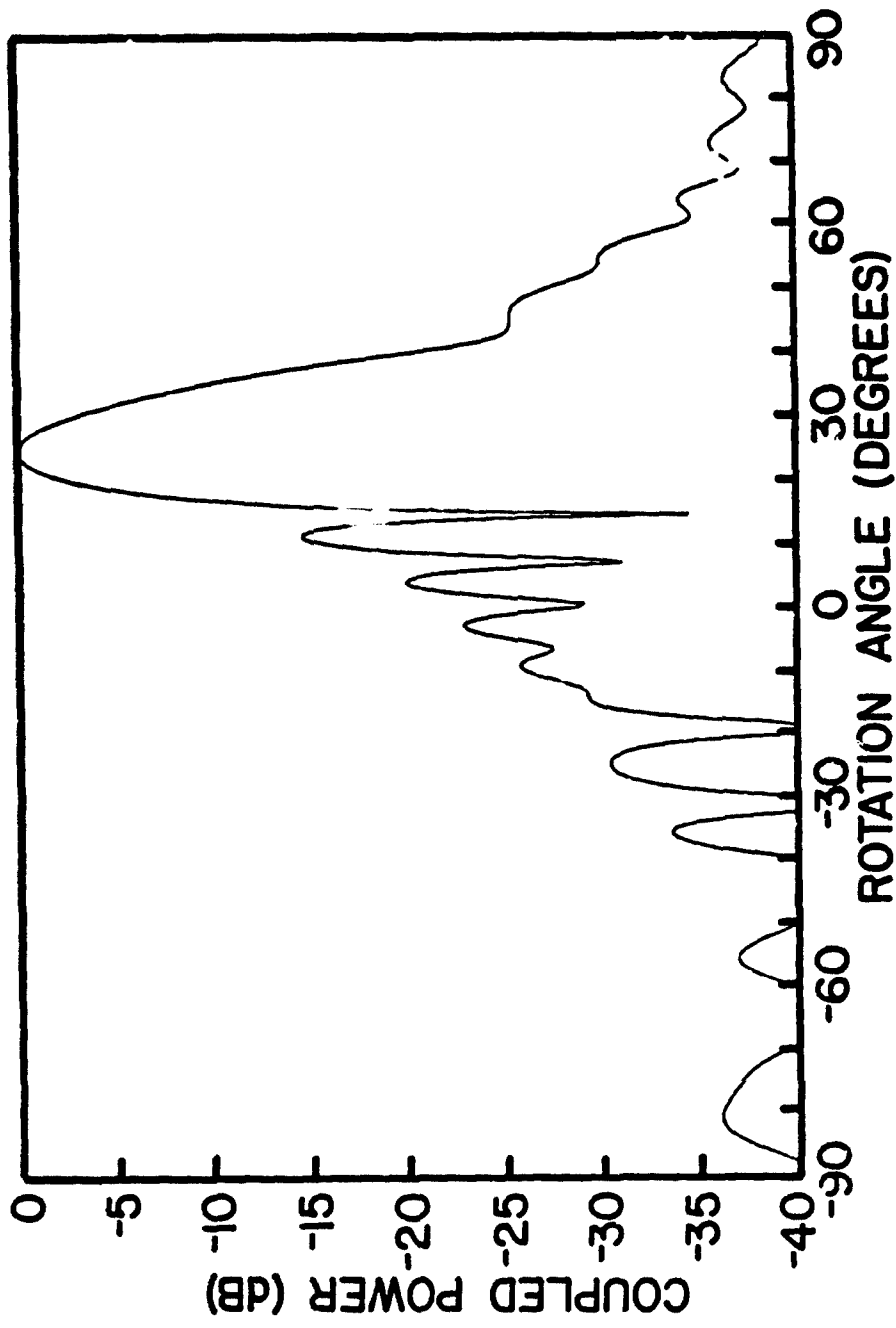
Figure 4-5. Coupled power versus rotation angle for a pair of 10-λ circular aperture antennas for a separation distance of 10λ for a skew angle of -26.0 degrees for integration over an integration range of 90 degrees.

46
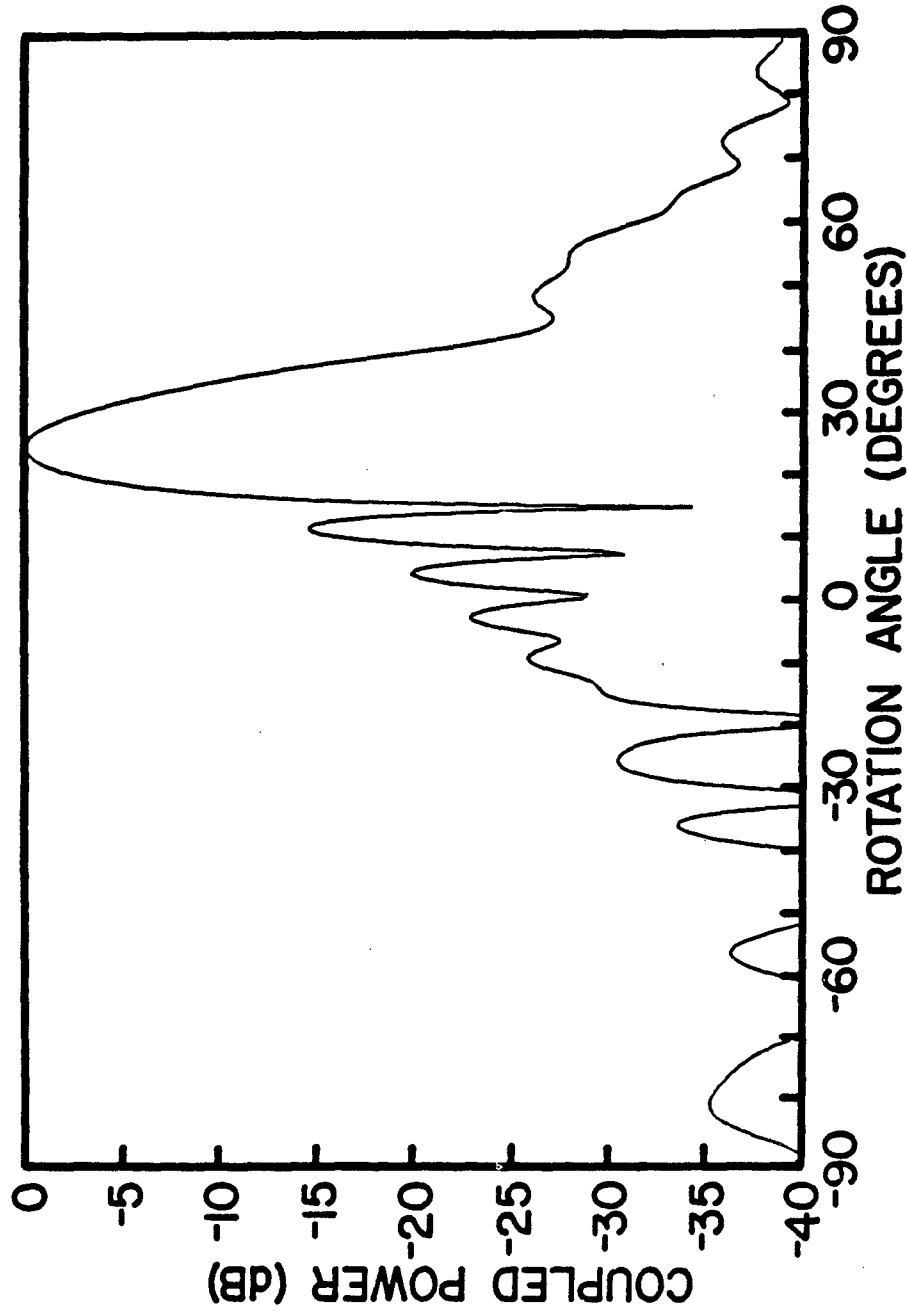
Figure 4-6. Coupled power versus rotation angle for a pair of 10-λ circular aperture antennas for a separation distance of 10λ for a skew angle of −26.0 degrees for integration over an integration range of 120 degrees.
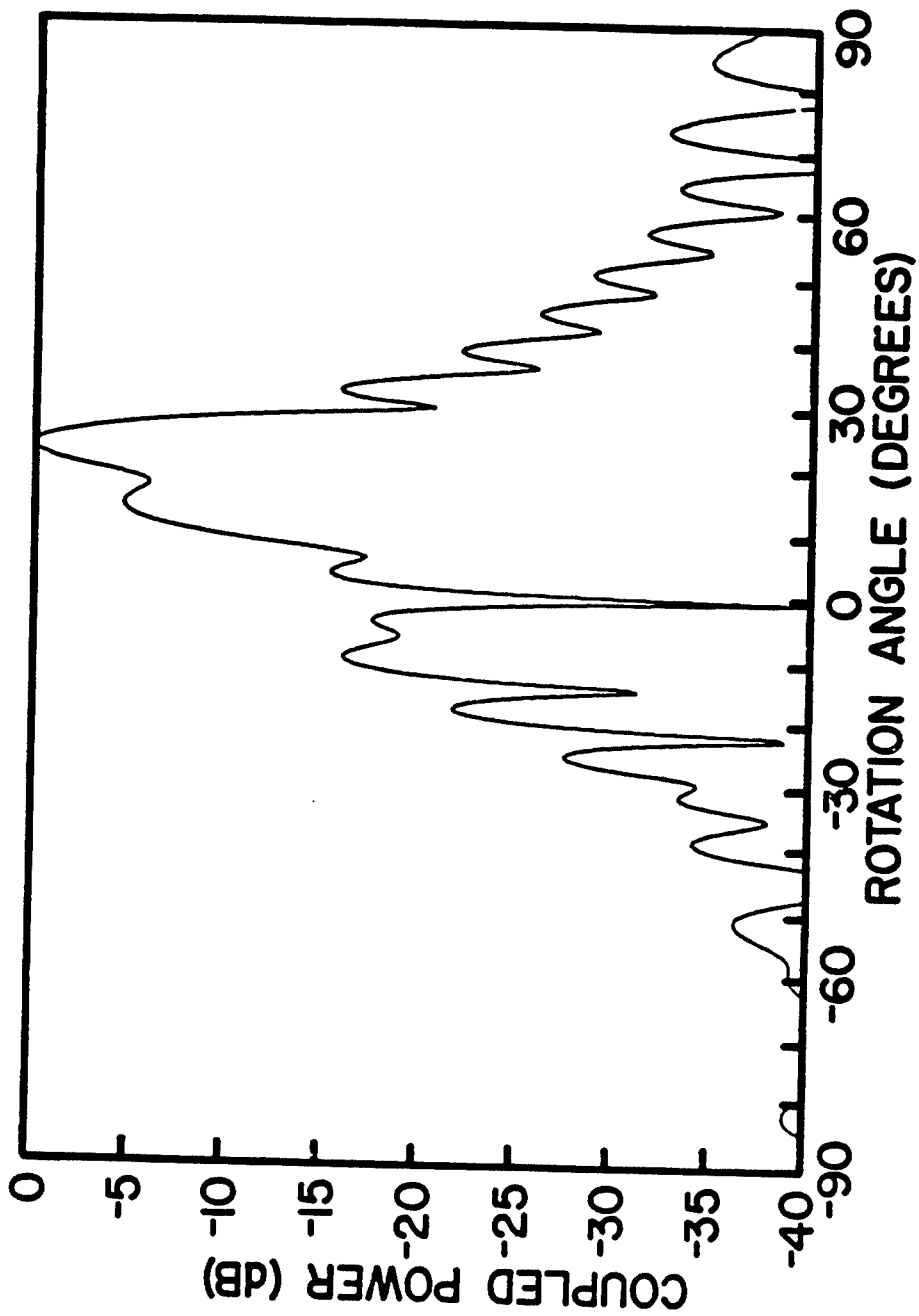
Figure 4-7. Coupled power versus rotation angle for a pair of 10-λ circular aperture antennas for a separation distance of 25λ for a skew angle of −26.0 degrees for integration over an integration range of 48 degrees.
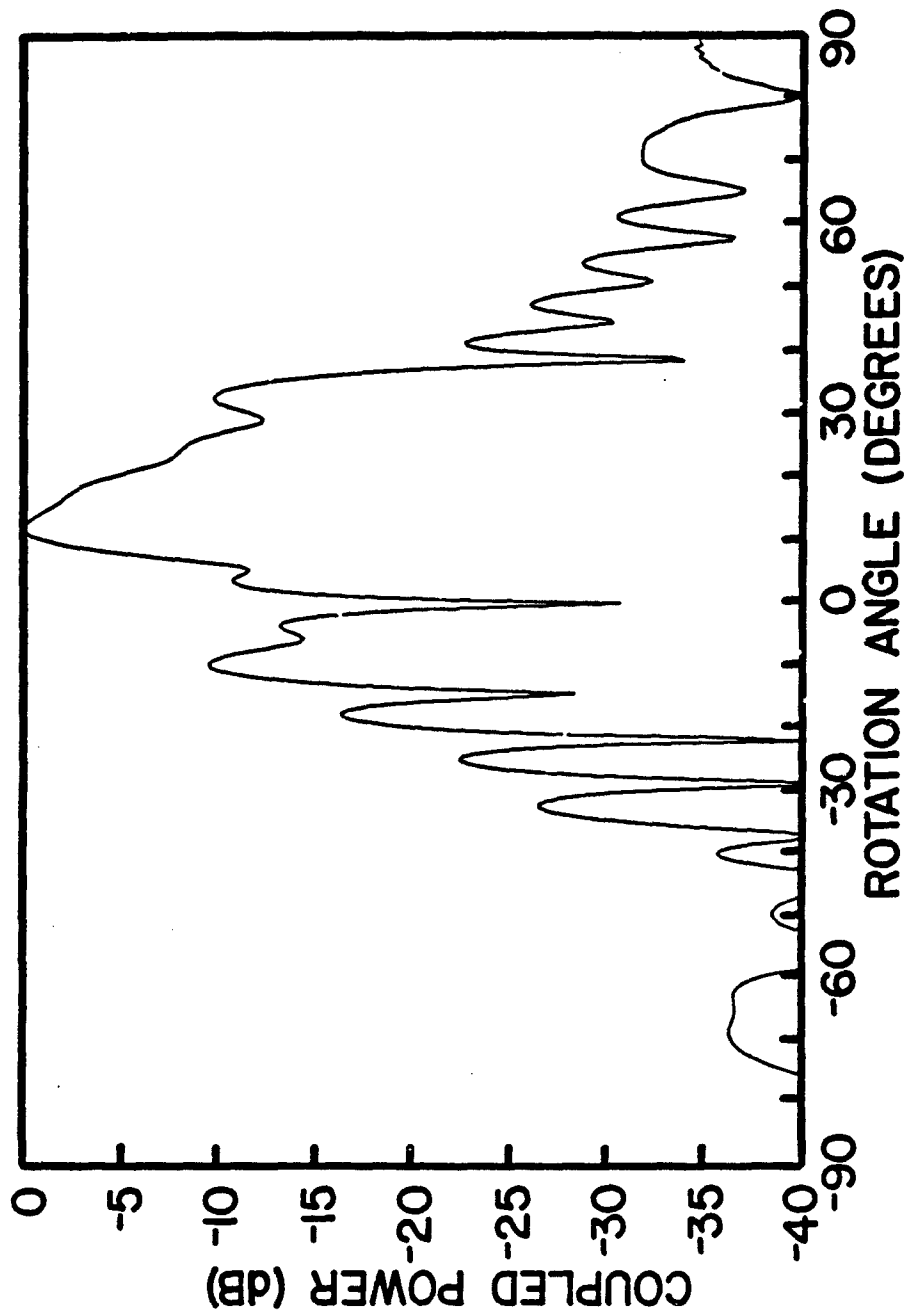
Figure 4-8. Coupled power versus rotation angle for a pair of 10-λ circular aperture antennas for a separation distance of 25λ for a skew angle of -26.0 degrees for integration over an integration range of 70 degrees.

49
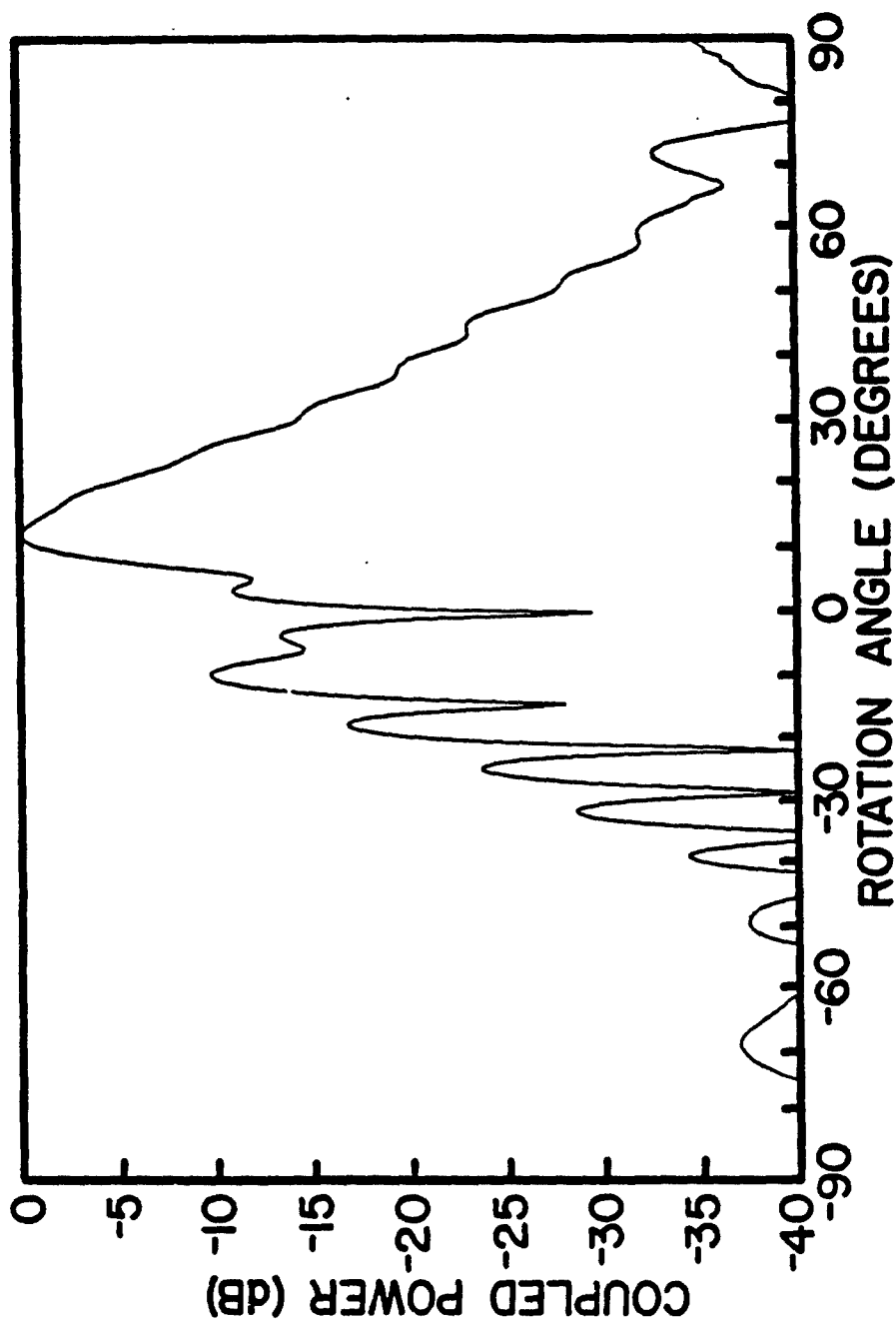
Figure 4-9.   Coupled power versus rotation angle for a pair of 10-λ circular aperture antennas for a separation distance of 25λ for a skew angle of -26.0 degrees for integration over an integration range of 90 degrees.
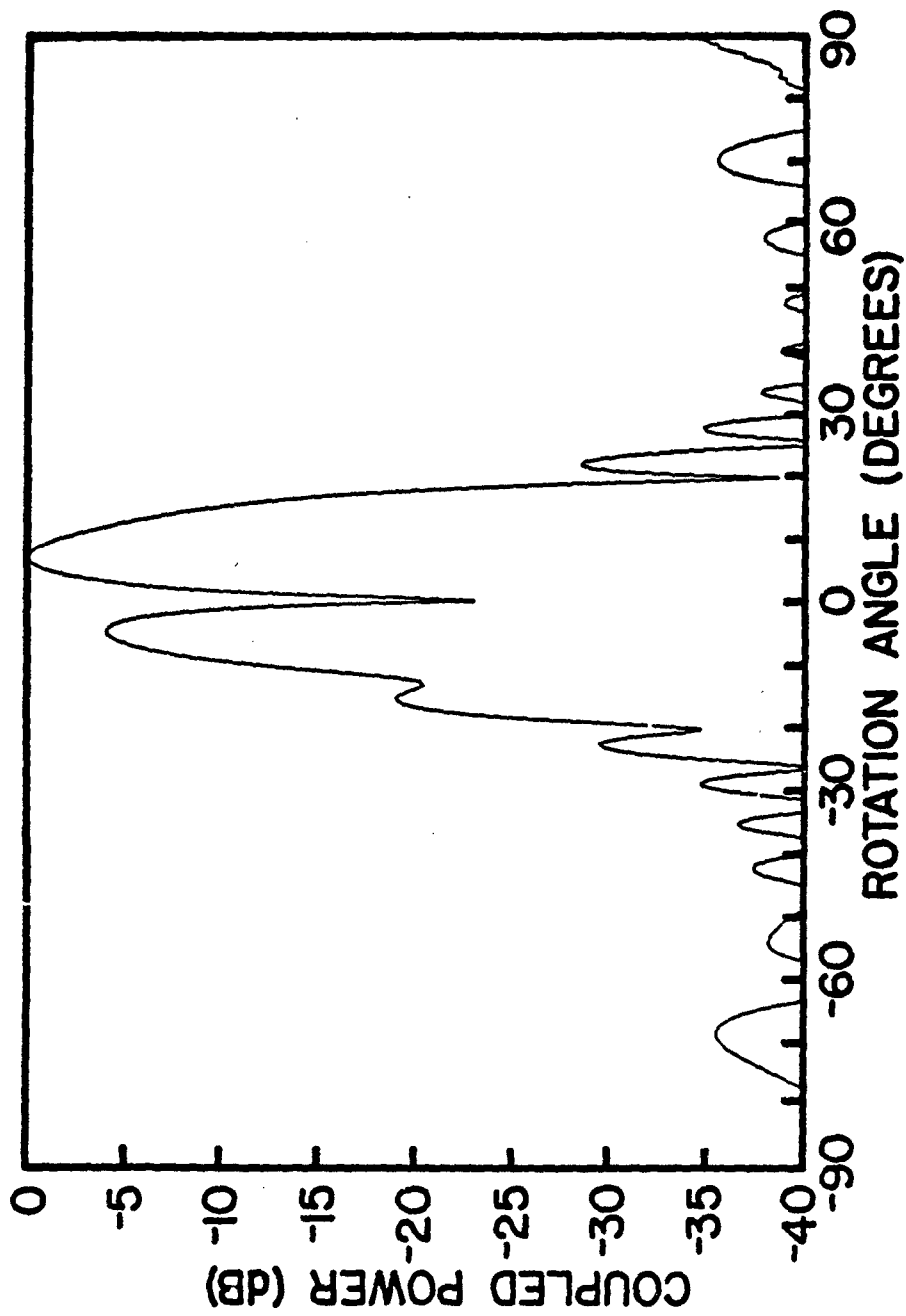
Figure 4-10. Coupled power versus rotation angle for a pair of 10-λ circular aperture antennas for a separation distance of 40λ for a skew angle of −26.0 degrees for integration over an integration range of 29 degrees.

51
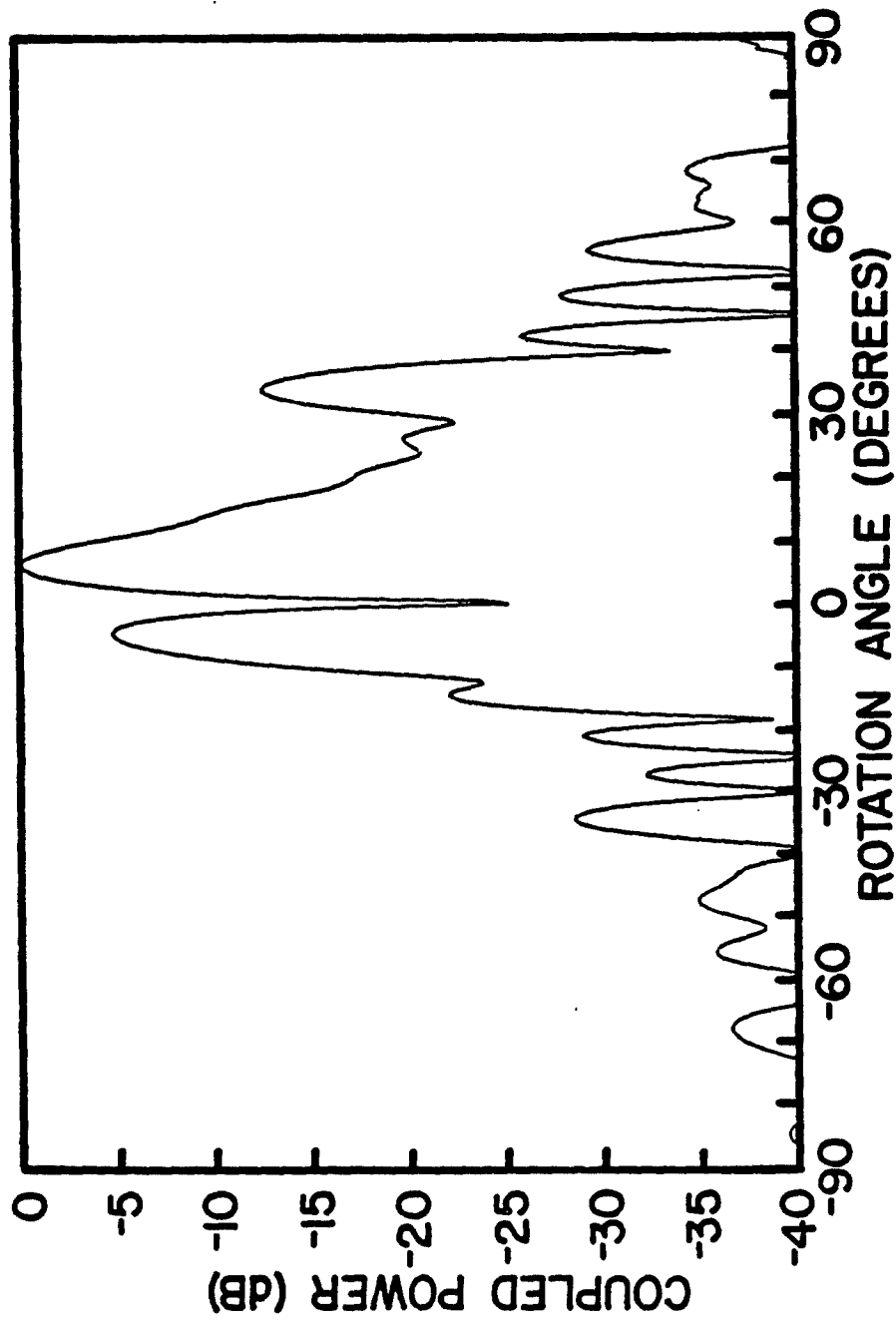
Figure 4-11. Coupled power versus rotation angle for a pair of 10-λ circular aperture antennas for a separation distance of 40λ for a skew angle of -26.0 degrees for integration over an integration range of 70 degrees.
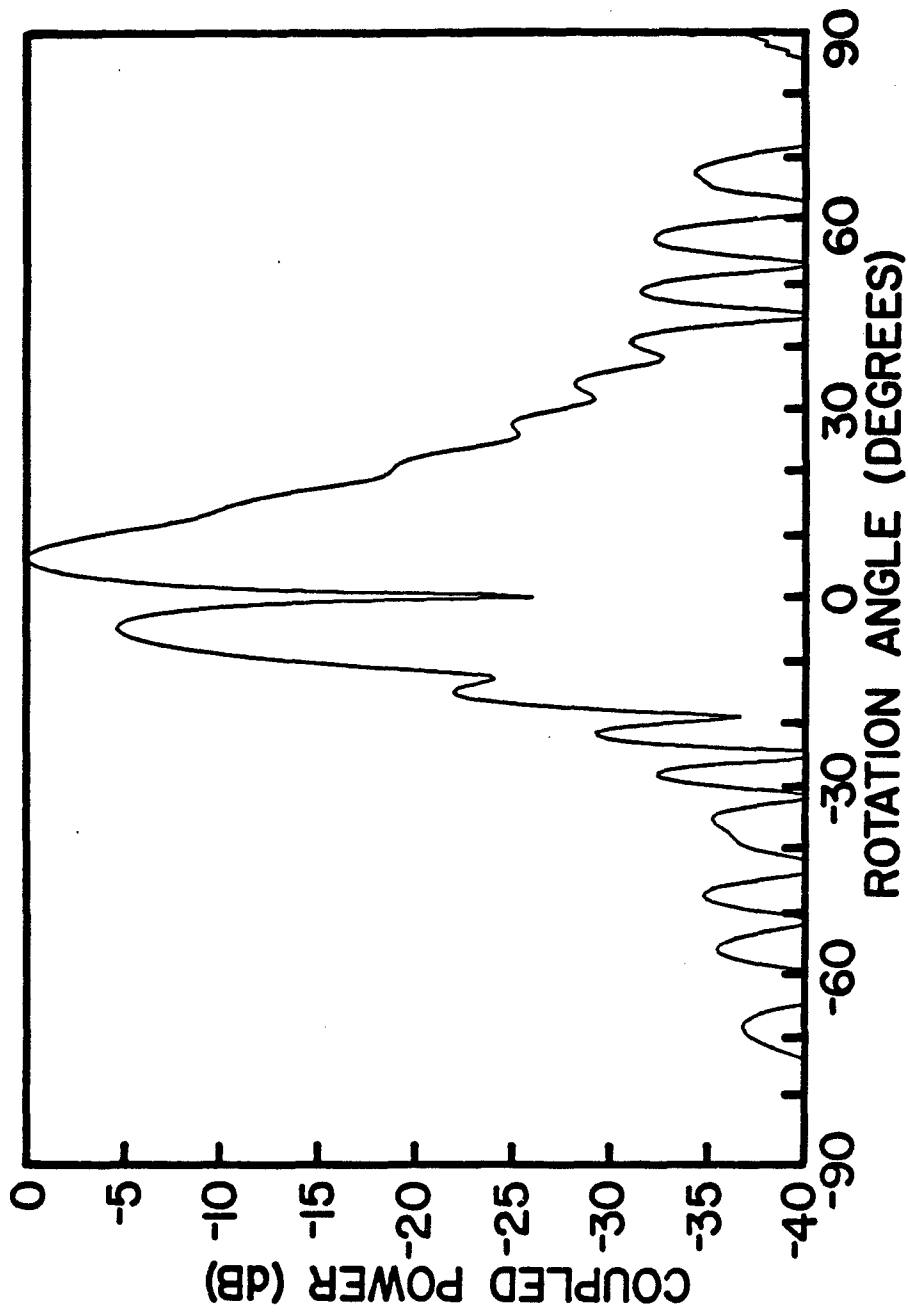
Figure 4-12. Coupled power versus rotation angle for a pair of 10-λ circular aperture antennas for a separation distance of 40λ for a skew angle of -26.0 degrees for integration over an integration range of 90 degrees.

separation distance. Each of the three curves for each separation distance was computed for the integration ranges specified in the caption.

Figures 4-4, 4-5, and 4-6 show the coupled power versus rotation angle for the 10-λ separation distance for integration over angular regions of total width 70 degrees, 90 degrees and 120 degress, consecutively. The 90 degree angle corresponds to the angle Θ_{sub} mutually subtended by this pair of antennas separated by 10λ, as computed from the formula

$$\Theta_{sub} = 2 \arctan \left[\frac{D_a + D_b}{2R} \right] \qquad (4-1)$$

where all symbols are as previously defined. The integration region of 70 degrees was chosen to investigate the impact on accuracy of using an integration region that extends beyond the mainbeam but that is smaller than the mutually subtended angle. The integration range of 120 degrees yields essentially the same coupled power curve as the one obtained by integrating over the entire front hemisphere as required by Equation (3-7). Inspection of these three curves shows that all three curves have their peak value occurring very near the rotation angle of $\beta = 26^{\circ}$ where the apertures of the two antennas are parallel. The computed peak values occur at 24.5°, 25.0°, 25.0° and for the integration ranges of 70 degrees, 90 degrees, and 120 degrees, consecutively. The curves for the integration ranges of 70 degrees and 90 degrees differ noticeably, but not drastically, from the curve for the 120 degree integration range. These limited results indicate that the integration range specified by Equation (3-7) yields a conservative guideline provided that the skew angle is much smaller than the angular half-width of the stationary phase region. The curves computed from the integration ranges of 70 degrees or 90 degrees may be accurate encugh for some EMC applications.

The curves presented in Figures 4-7 through 4-9 for a separation distance of 25λ and those presented in Figures 4-10 through 4-12 for a separation distance of 40λ further illustrate general trends and provide additional understanding of the impact of the integration region on computational accuracy. One notes that the peak value of coupled power has shifted progressively closer to the stationary phase direction, which coincides with a rotation angle of $\beta = 0$ degrees on the plots, as the

54

separation distance has been increased. In particular, the peak value for the most accurately computed curve (i.e., the one obtained with the largest integration region) for each separation distance occurs at an angle of about 25 degrees, 12 degrees, and -3 degrees for the separation distances of 10λ, 25λ, and 40λ, consecutively. This is a sensible trend which implies the well known result that for very large separation distances the power coupled to the receiving antenna is maximum when its mainbeam is pointed directly at the transmitting antenna.

A significantly sensitivity in the computed curves to the size of the integration range may be discerned by inspecting the curves for the separation distances of 25λ and 40λ. The integration range of 48 degrees determined from Equation (3-7) for the separation distance of 25λ is also approximately the angle mutually subtended by these two antennas for that separation distance. Similarly, the integration range of 29 degrees for the separation distance of 40λ is also approximately the angle mutually subtended by the two antennas for that separation distance. The integration range of 70 degrees provides integration over a cone of half angle equal to 35 degrees which extends considerably beyond the peak of the skewed transmitting (far-field) mainbeam. The integration region of 90 degrees yields coupled power plots that have essentially converged to a stable result. Thus, it was necessary to integrate over a range almost twice the size of the stationary phase region for the separation distance of 25λ and to integrate over a range almost three times the size of the stationary phase region for the separation distance of 40λ when the transmitting antenna is skewed at $\xi_o = -26$ degrees.

These results provide useful insight into general coupling trends and the impact of the size of the integration region on computational accuracy. However, it should be recognized that some aspects of both the general trends and the sensitivity of the computational accuracy to the integration range may depend significantly on the aperture distribution and, hence, on the far-field pattern. Accordingly, it would be useful to conduct similar numerical studies involving other pattern functions.

C. GTSAF Coupling Calculations and Experimental Data

A sample execution for the antenna coupling algorithm GTSAF is presented in Figure 4-13. GTSAF is designed to accept complex input

```
"PROGRAM GTSAF COMPUTES THE NEAR FIELD MUTUAL"
"GAIN FOR A PAIR OF ANTENNAS OPERATING EITHER ON"
"A CLEAR SITE OR IN THE PRESENCE OF A TALL ROUND MAST OR SHEET"
"OBSTACLE.  THE PROGRAMS EHPARAB AND GTOBS CAN BE USED TO"
"GENERATE THE INPUT ANTENNA AND THE ANTENNA/SCATTERER"
"DATA FILES REQUIRED BY GTSAF "

"LINEAL DIMENSIONS ARE IN FEET"

"ENTER DIAMETER OF CIRCUMSCRIBING SPHERE FOR ANTENNA A"
?
 4.
"ENTER DIAMETER OF CIRCUMSCRIBING SPHERE FOR ANTENNA B"
?
 4.
"ENTER FREQUENCY IN GHZ"
?
 5.5
"ENTER THE DISTANCE BETWEEN THE ANTENNAS"
?
 16.8
"ENTER ANGULAR COORDINATES OF ANTENNA A WITH RESPECT"
"TO ANTENNA B"
?
 90.
?
 0.
"ENTER THE AZIMUTH OFFSET ANGLE FOR ANTENNA A"
?
 0.
"ENTER ANTENNA B AZIMUTH ROTATION ANGLE LIMITS"
?
 -24.
?
 24.
"ENTER ANGULAR INCREMENTS FOR ROTATION ANGLE"
?
 1.
"END OF EXECUTION.  OUTPUT MUTUAL GAIN DATA"
"IS IN FILE MGOUT."
```

Figure 4-13. Sample execution for the antenna coupling computer
program GTSAF for the computed data plotted in
Figure 4-15.
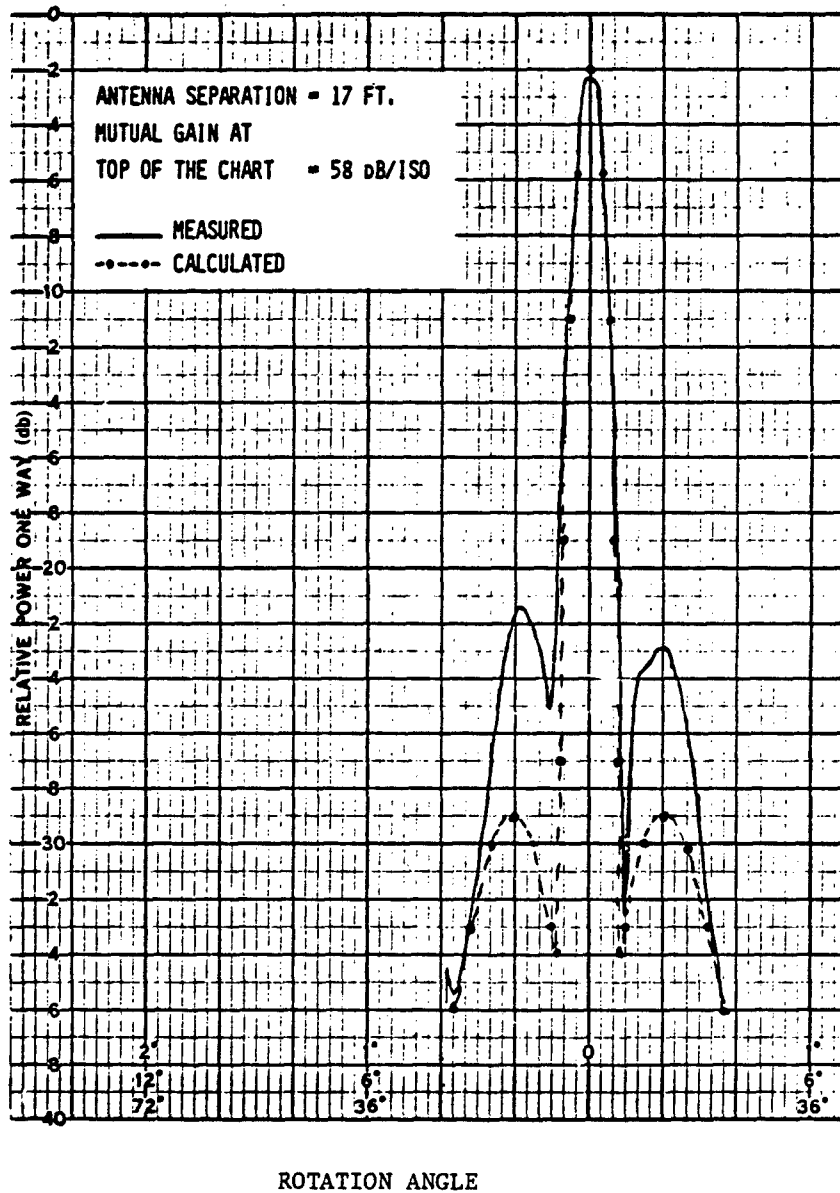
ROTATION ANGLE

Figure 4-14. Antenna coupling versus antenna rotation angle for the near-field situation depicted in the inset of Figure 4-15 with the round mast obstacle removed, i.e., on a "clear site."
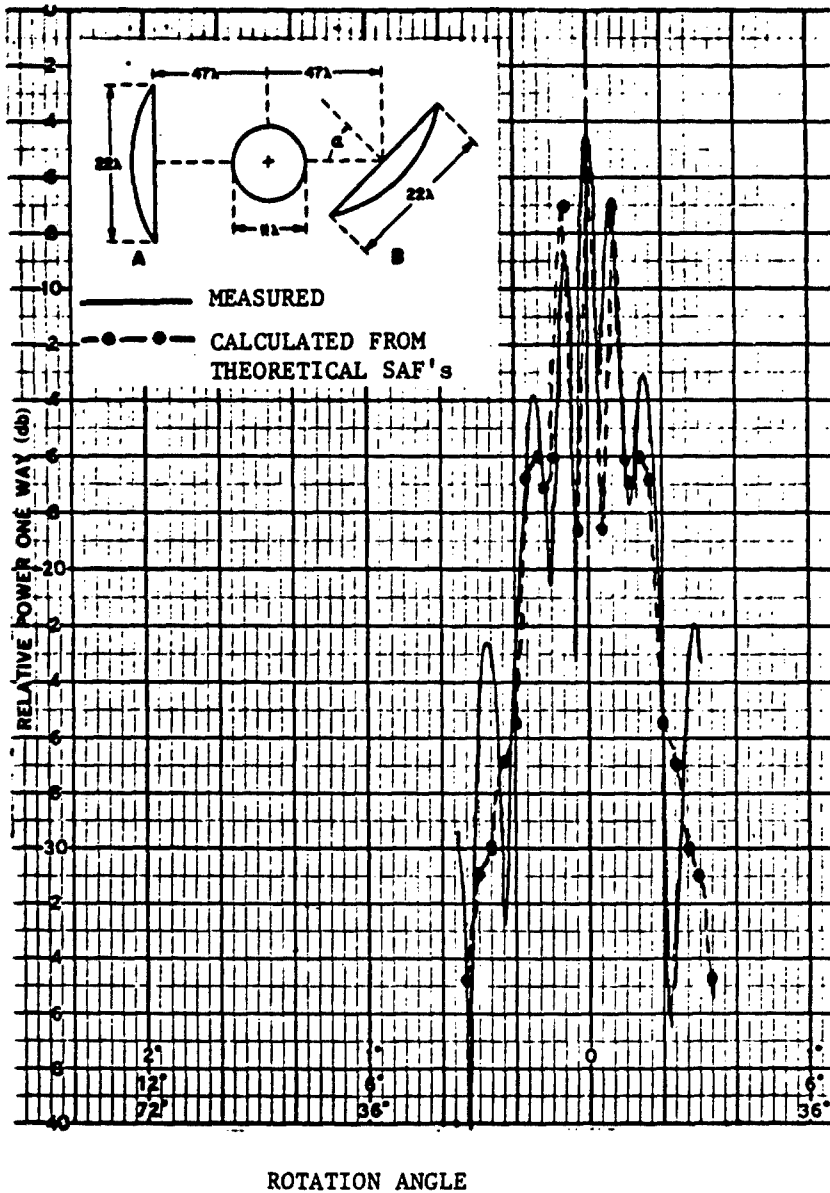
ROTATION ANGLE

Figure 4-15. Antenna coupling versus antenna rotation angle
for the near-field situation depicted in the
inset for 5.5 GHz.

antenna data and/or composite antenna/obstacle data that has been measured or data that has been generated from an auxiliary program. The GTSAF algorithm can be employed to compute near-field power coupling for pairs of reflector antennas, wire antennas, horn antennas, and phased arrays. Coupling between these different types of antennas can be based on a knowledge of their SAF's. The GTSAF results for two reflector antennas operating on a clear-site and in the presence of a round mast obstacle are shown in Figures 4-14 and 4-15, respectively. The measured coupling data ior Figures 4-14 and 4-15 were obtained during a previous Navy contract. The GTSAF coupling data for these two figures were obtained by using theoretical SAF's, as follows. First, the obstacle effects program GTOBS was employed to generate both clear-site and blocked pattern data. Cosine-on-a10-dB pedestal aperture illumination functions were used for the two reflectors. The GTOBS computer SAF data were then used as input data to GTSAF to compute the coupling data displayed in Figures 4-14 and 4-15. Inspection of the antenna coupling for the blocked situation shown in Figure 4-15 reveals that a good engineering description of the measured coupled power is obtained from GTSAF despite the fact that the computed unobstructed coupled power data do not closely replicate the "sidelobes" of the measured unobstructed power coupling data displayed in Figure 4-14.

D. Auxiliary Programs GTOBS and EHPARAB

Program GTOBS is designed to accept antenna patterns generated from EHPARAB and to complete blocked patterns using either cylinders or flat plates as the scattering obstacles located near the antenna. These patterns then can be written to files for use as input to the mutual coupling program GTSAF. Initial input to GTOBS is partially from files and partially interactive. It is assumed that before program execution elevation and azimuthal antenna patterns are contained in complex form in files ANTEL and ANTAZ, respectively. Each complex value is preceded by the corresponding theta or phi angle. The first column of the elevation file contains an elevation cut for the front hemisphere, i.e., $\phi = 0^\circ$, $0^\circ < \theta < 180^\circ$. The second column contains a similar cut for the back hemisphere, for $\phi = 180^\circ$, $0^\circ < \theta < 180^\circ$. The azimuthal file contains an azimuth cut for the entire $\theta = 90^\circ$ plane, $0^\circ < \phi < 360^\circ$. The initial interactive input is mostly concerned with the physical parameters of the

59

situation for which a pattern is to be computed. Information such as the width of the antenna, the position of the obstacle relative to the antenna, and the shape and size of the obstacle is input in this section.

EHPARAB is used to compute the E-plane and H-plane patterns of a horn-fed parabolic dish antenna over complete circles encompassing the antenna. EHPARAB is based on the "physical optics" integral over the reflector current distribution, as described by Silver in Microwave Antenna Theory and Design. The computed complex electric field data are then used in GTOBS to compute composite antenna/scatterer patterns and in GTSAF to compute antenna coupling. Plots of the computed amplitude of the electric field scattered from the reflector dish due to illumination by a short dipole located at the focus are shown in Figure 4-16 and 4-17 for the E-and H-planes, respectively. The EHPARAB data precisely match other published data for this case. The operator inputs to EHPARAB are frequency, the F/D ratio for the dish, the peak gain and the principal plane pattern functions of the feed horn, and the direction of the assumed linear polarization of the feed horn.
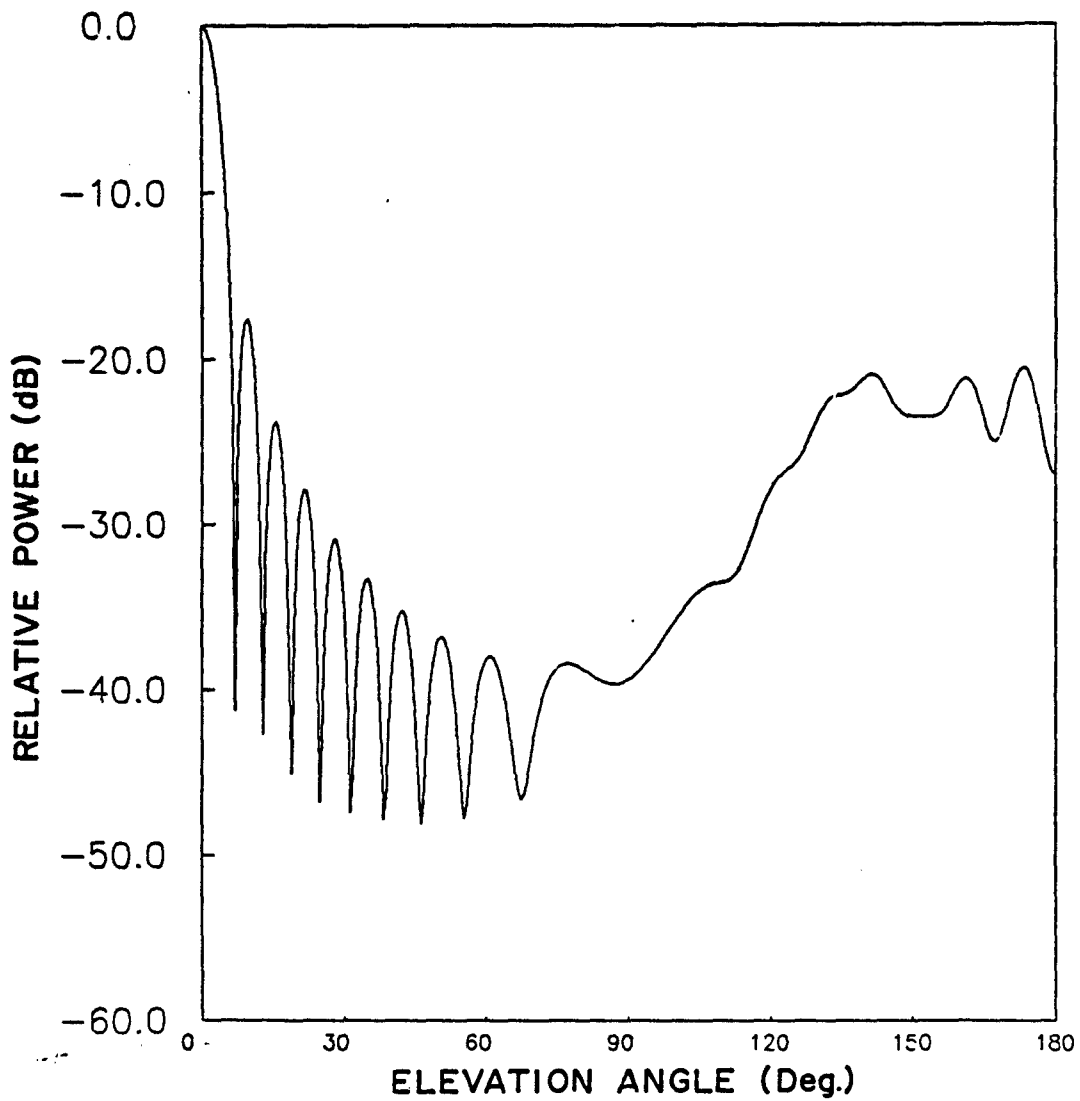
Figure 4-16. E-plane scattered pattern for a reflector
antenna fed by a short dipole for F/D = 0.43,
D = 10 wavelengths.
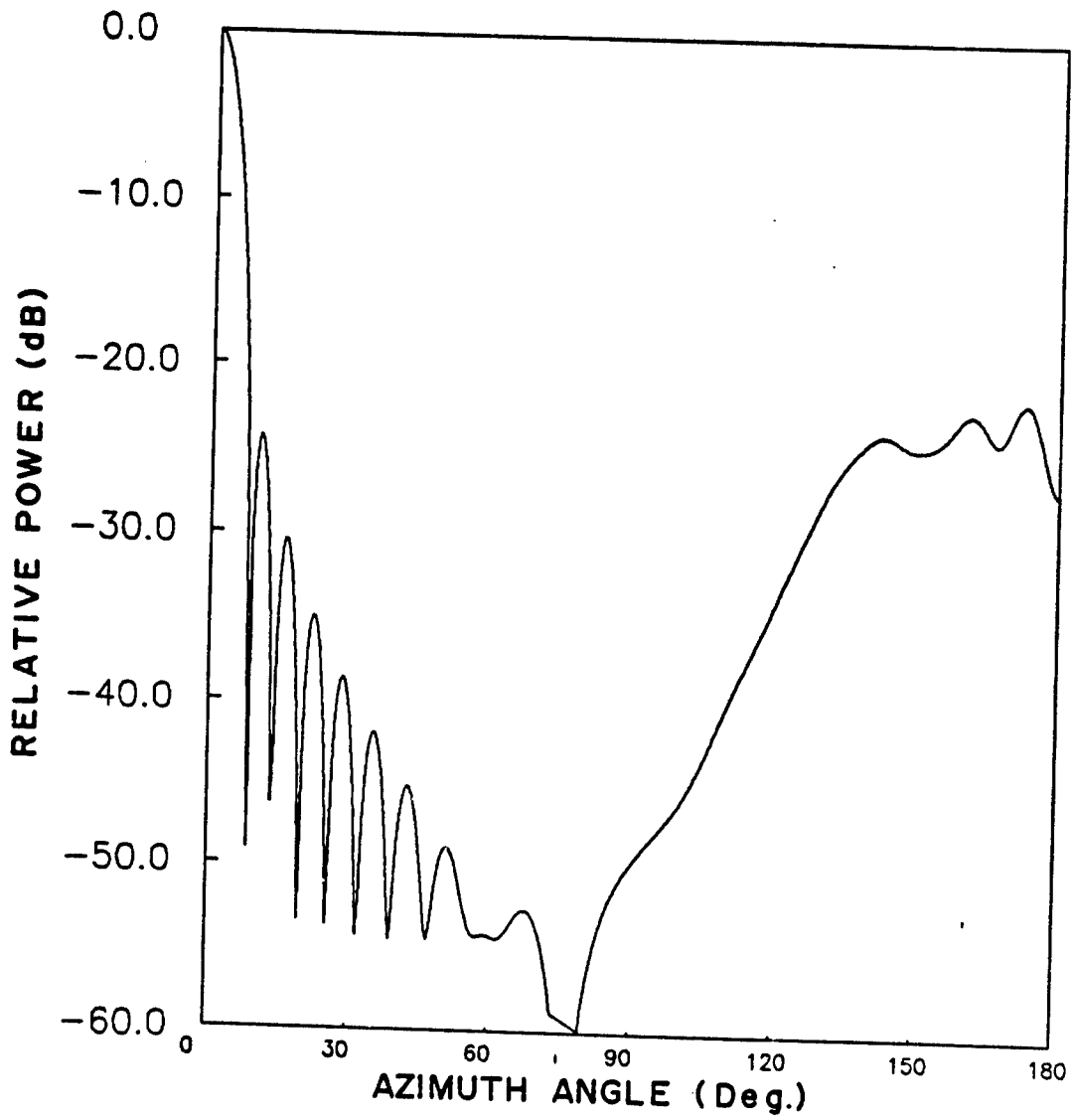
Figure 4-17.   H-plane scattered pattern for a reflector
antenna fed by a short dipole for F/D = 0.43
and D = 10 wavelengths.

SECTION V
CONCLUDING REMARKS AND RECOMMENDATIONS

The efforts to develop an efficient and versatile computer algorithm for computing antenna coupling in the presence of near-field obstacles were successful. The results of the analytical and numerical research work show that the algorithm based on the Spherical Angular Function (SAF) technique can be used for applications involving antennas of low, moderate and/or high directivity.

The basic SAF equations were first derived for describing clear-site antenna coupling in terms of the normalized SAF's of the antennas. The normalized SAF F_o (θ,ϕ) of an antenna is related to the far-field complex electric field $E_{ff}(\theta,\phi)$ of the antenna as $F_o(\theta,\phi) = [g]^{-\frac{1}{2}} re^{jkr}E_{ff}(\theta,\phi)$, where r is the far-field range of the observation point and g is the peak far-field gain of the antenna. The coupling analysis requires the evaluation of double convolution integrals involving the SAF's of the two antennas over portions of the far-field sphere, where the notion of convolution was extended to include the type of integrals encountered in near-field antenna coupling analysis. The corresponding SAF equations for antennas operating in the presence of near-field scattering obstacles were also derived.

Numerical data are calculated and studied to determine the general capabilities of the SAF-based antenna coupling algorithm and two related auxiliary algorithms. Firstly, coupling data were computed for a pair of $\frac{1}{2}-\lambda$ dipoles and for a pair of $10-\lambda$ circular aperture antennas. Secondly, mutual coupling data were calculated for a pair of directive antennas for clear-site as well as blocked conditions in the near-field. Good agreement was obtained between measured and computed data. The coupling program is denoted as GTSAF, and is supplied to CECOM under separate transmittal. The auxiliary program GTOBS and EHPARAB, for computing composite antenna/obstacle SAF's and for generating SAF's for paraboloidal reflector antennas, respectively, were also implemented and validated.

It would be particularly beneficial to CECOM for Georgia Tech (1) to make certain refinemets and extensions of the coupling prediction capabilities developed under this contract and (2) to obtain additional

63

measured data for model validations. Accordingly, the following research tasks are proposed in order to provide additional, validated analytical capabilities to CECOM for monitoring and improving EMC:

Task 1. Rapid Determination of SAF's for Antennas, Scatterers, and Equipments. The SAF's of antennas, scatterers, or equipments may be readily computed from the complex field data obtained from Near-field (NF) measurements. The feasibility of exploiting the Modulated Scattering Technique (MST) to develop a portable near-field test facility, capable of acquiring the NF data in a few minutes or seconds, should be investigated. A rapid NF measurement capability combined with the GTSAF algorithm will significantly enhance CECOM's ability to determine and control EMI.

Task 2. Out-of-Band Computer Model Simulations. A Monte Carlo computer model has been developed under a previous government contract to compute statistical average out-of-band reflector antenna patterns. Preliminary computer simulations have demonstrated that the out-of-band patterns are particularly sensitive to the relative phase deviation of the higher-order transmission line mode. However, the sensitivity of the model results as a function of variables such as the mode amplitudes mode phases, and "mixture" of modes has not yet been tested against measured data. It is proposed that the following numerical simulations be performed to determine the computer model sensitivity:

a. Exercise the computer model to determine the effects of mode amplitudes, mode relativae phases, and mode mixture on the out-of-band pattern statistics -- specifically, the mean pattern and standard deviations.

b. Modify the model to account for the effects of waveguide feed system length on the relative model phases by using the higher-order mode phase velocity equations.

c. Compare the computer model mean patterns and standard deviations with the measured data obtained during the measurement program.

Task 3. Extension of the Out-of-Band Reflector Antenna Pattern Model. The present computer model performs a vector calculation of the average

64

pattern and standard deviation over an approximately $\pm50^{\circ}$ to $\pm80^{\circ}$ field-of-view centered on the antenna boresight. In many applications, it is desirable to determine the complete pattern statistics including the back-lobe regions. Also, it is often necessary to compute pattern statistics such as the median gain and standard deviation over either a complete 4π steradian or partial angular sector. However, with the present model, these computations can be time-consuming and expensive. Thus, it is proposed that the model be extended to:

a. Include the effects of reflector rim edge diffraction and strut and feed horn blockage on the out-of-band antenna pattern. This extension will make it possible to compute the out-of-band pattern over a full 4π steradian angular sector, or over any selected subsector of the pattern.

b. Incorporate routines to determine the median gain and standard deviation of the out-of-band pattern for the full 4π steradian angular sector.

c. Examine computational methods to decrease the computer run time required by the model. These methods might incorporate some recently published techniques which are particularly suited to circular aperture-type antennas.

Task 4. Additional Out-of-Band Pattern Measurements. Additional measurements of the out-of-band pattern performance of reflector antennas are needed to determine the effects of transmission line components. The out-of-band pattern performance has been shown to be sensitive to the type of waveguide transmission components employed in the feed system. To date, measurements have been performed using a simple coaxial cable-to-waveguide adapter feed system. It is proposed that additional measurements be performed using a feed system incorporating:

a. coaxial cable-to-waveguide adapter and E-plane bend,

b. coaxial cable-to-waveguide adapter and H-plane bend,

c. a coaxial cable-to-waveguide adapter attached to a typical waveguide feed which extends from the reflector rim to the feed horn.

65

Statistical processing will be performed on the data to determine whether the different transmission line devices result in significant changes in the out-of-band statistical average pattern performance. These measurements will be performed over frequency bands centered about the fundamental, the second, and the third harmonic frequencies.

Task 5. Out-of-Band Antenna Coupling. Very little measured data are available validate out-of-band data computed via GTSAF. It is, therefore, proposed to perform a limited set of out-of-band antenna coupling measurements, including the following:

a. Out-of-band coupling measurements as a function of azimuth angle for two reflector antennas located at the same elevation. (Note: this corresponds to the "common boresight" case.) These measurements will be performed over frequency bands centered on the second and third harmonics.

b. Antenna coupling measurements as a function of azimuth angle for two reflector antennas separated by approximately one-to-two antenna diameters in elevation. These measurements will be performed over frequency bands centered on the second and third harmonics.

The measured data will be processed to determine the mean and standard deviation of the out-of-band coupling as a function of azimuth angle.

SECTION VI

REFERENCES

1. R. F. Harrington, Field Computation by Moment Methods, MacMillan Co., New York 1968.

2. A. T. Adams, "Method of Moments Applications-Vol. I., An Introduction to the Method of Moments," RADC-TR-73-217, November 1974, AD #A-002820.

3. R. C. Hansen, Microwave Scanning Antennas, Volume I, Academic Press, New York, 1964.

4. F. L. Cain, C. E. Ryan, B. J. Cown, and E. E. Weaver, "Electromagnetic Effectiveness Investigations of Near-Field Obstacle Effects, Antenna Coupling and Phased Arrays," Georgia Institute of Technology, Final Engineering Report, Contract No. N00024-72-C-1276.

5. R. C. Rudduck and R. J. Markefka, "Quasi-Optical Techniques for Antennas at UHF and Above," Ohio State University ElectroScience Laboratory, Quarterly Report 712242-6, Contract No. N00123-79-C-1469, February 1981.

6. B. Ye. Kinber, "Decoupling of Closely Situated Reflector Aerials," Radiotekhnika i Electronika 6, No. 6, 1961, pp. 907-916.

7. E. Schweicher, "Linkage Between Two Microwave Antennas in the Presence of a Cylindrical Reflector," Annales Des Telecommunications, Tome 34, Nos. 9-10, September-October 1979.

8. C. E. Ryan, Jr., E. E. Weaver, and W. P. Cooke, "Development of Total Electromagnetic Effectiveness During Ship Design," Georgia Institute of Technology, Final Technical Report, Contract No. N00024-77-C-5338, December 1979.

9. C. E. Ryan, Jr., E. E. Weaver, and B. J. Cown, "Plane Wave Spectrum Analysis of Near-Field Obstacle Effects on Directive Antenna Patterns," IEEE Transactions on Antennas and Propagation, 27, No. 6, November 1979.

10. B. J. Cown and C. E. Ryan, Jr., "Near-Field Theory and Techniques for Wideband Radiating System at In-Band and Out-of-Band Frequencies," Georgia Institute of Technology, Final Technical Report, Contract No. DAAG29-78-C-0029, January 1982.

11. A. D. Yaghjian, "Efficient Computation of Antenna Coupling and Fields Within the Near-Field Region," IEEE Transactions on Antennas and Propagation, Volume AP-30, No. 1, pps. 113-128, January 1982.

12. B. J. Cown, "In-Band Antenna Coupling Research," Georgia Institute of Technology, Interim Technical Report No. 1, Contract DAAB07-82-C-J069, September 30, 1982.

13. G. D. Bergland, "A Guided Tour of the Fast Fourier Transform," IEEE Spectrum, July 1969.

14. D. M. Kerns, Plane Wave Scattering Matrix Theory of Antenna and Antenna-Antenna Interactions, U. S. Government Printing Office, Library of Congress Catalog Card Number: 81-600015, June 1981.

15. V. H. Rumsey, "Reaction Concept in Electromagnetic Theory," Physical Review, Volume 94, No. 6, pp. 1483-1491, June 15, 1954.

16. R. F. Harrington and A. T. Villeneuve, "Reciprocity Relationships for Gyrotropic Media," IRE Transactions on Microwave Theory and Techniques, MTT-6, pps. 308-310, July 1958.

17. Microwave Antenna Theory and Design, S. Silver (Editor), Dover Publications, New York, 1965.

18. P. M. Morse and H. Feshbach, Methods of Theoretical Physics, Volume 2, McGraw-Hill Book Co., New York, 1953.

19. A. Banos, Jr., Dipole Radiation in the Presence of a Conducting Half-Space, Pergamon Press, New York, 1966.

20. L. Schwartz, "Theorie des Distributions a Valeurs Vectorielles," Annales de L'Institut Fourier, Universite de Grenoble, Tome 8-9, 1958-1959, pp. 1-202.

21. L. Schwartz, Mathematics for the Physical Sciences, Addison-Wesley Publishing Co., Reading, Massachusetts, 1966.

22. N. Zittron and S. N. Karp, "Higher Order Approximations in Multiple Scattering II. Three Dimensional Scalar Case," Journal of Mathematical Physics, Vol. 2, No. 3, May-June 1961.

23. K. Hongo, "Multiple Scattering by Two Conducting Circular Cylinders," IEEE Antennas and Propagation, Vol. AP-26, No. 5, September 1978.

24. P. Debeye, "Approximate Formulae for the Cylinder Functions for Large Values of the Argument and Any Value of the Index," The Collected Papers of Peter J. W. Debeye, Interscience Publishers, Inc., New York, 1954.

25. P. M. Morse and H. Feschback, Methods of Theoretical Physics, Volume 1, McGraw-Hill Book Co., New York, 1953.

APPENDIX A

DISTRIBUTION LIST

DISTRIBUTION LIST

Address	No. of Copies
* Defense Technical Information Center ATTN: DTIC-FDAC Cameron Station (Bldg 5) Alexandria, VA 22304-6145	*
Director National Security Agency ATTN: TDL Fort George G. Meade, MD 20755	01
DCA Defense Communications Engineering Center CODE R123, Tech Library 1860 Wiehle Avenue Reston, VA 20090	01
Defense Communications Agency Technical Library Center CODE 205 (P.A. TOLOVI) Washington, DC 20305	02
Commanding Officer Naval Research Laboratory ATTN: CODE 2627 Washington, DC 20375	01
Commander Naval Ocean Systems Center ATTN: Library San Diego, CA 92152	01
Commander Naval Surface Weapons Center White Oak Laboratory ATTN: Library, CODE WX-21	01
Commandant Marine Corps ATTN: CODE LMC Washington, DC 20380	02
Headquarters US Marine Corps ATTN: CODE INTS Washington, DC 20380	01

(*Note to contractor: These 2 copies will be sent from the STINFO Office, Fort Monmouth, N.J.)

DISTRIBUTION LIST (CONTD)

Address	No. of Copies
Command, Control & Communications Division Development Center Marine Corps Development & Education Command Quantico, VA 22134	01
Naval Telecommunications Command Technical Library, CODE 9IL 4401 Massachusetts Avenue, NW Washington, DC 20390	01
Naval Air Systems Command CODE: AIR-5332 Washington, DC 20360	04
Dr. T. G. Berlincourt Office of Naval Research (CODE 420) 800 N. Quincy Street Arlington, VA 22217	01
AUL/LSE 64-285 Maxwell AFB, AL 36112	01
Rome Air Development Center ATTN: Documents Library (TSLD) Griffiss ARB, NY 13441	01
USAFETAC/CBTL ATTN: Librarian STOP 825 Scot AFB, IL 62225	01
Air Force Geophysics Lab L. G. Hanscom AFB ATTN: LIR Bedford, MA 01730	01
AFGL/SULL S-29 HAFB, MA 01731	01
Headquarters AFEWC ATTN: EST San Antonio, TX 78243	02

DISTRIBUTION LIST (CONTD)

Address	No. of Copies
Headquarters Air Force Systems Command ATTN: DLWA/Mr. P. Sandler Andres AFB Washington, DC 20331	01
Commander MICOM Redstone Scientific Information Center ATTN: Chief, Document Section Redstone Arsenal, AL 35309	02
Commander MICOM ATTN: DRSMI-RE (Mr. Pittman) Redstone Arsenal, AL 35809	01
Commandant US Army Aviation Center ATTN: ATZQ-D-MA Fort Rucker, AL 36362	01
Commander Headquarters Fort Huachuca ATTN: Technical Reference Division Fort Huachuca, AZ 85613	01
Commander US Army Electronic Proving Ground ATTN: STEEP-MT Fort Huachuca, AZ 85613	01
Commander US Army Proving Ground ATTN: STEYP-MTD (Tech Library) Yuma, AZ 85364	01
Director US Army Air Mobility R&D Lab ATTN: T. Gossett, Bldg 207-5 Nasa Ames Research Center Moffett Field, CA 94035	01
HQDA (DAMO-TCE) Washington, DC 20310	02

DISTRIBUTION LIST (CONTD)

Address	No. of Copies
Deputy For Science & Technology Office, Asst Sec Army (R&D) Washington, DC 20310	02
HQDA (DAMA-ARZ-D/Dr. F. D. Verderame) Washington, DC 20310	01
Commandant US Army Signal School ATTN: ATSH-CD-MS-E Fort Gordon, GA 30905	01
Commandant US Army Infantry School ATTN: ATSH-CD-MS-E Fort Benning, GA 31905	01
Commander ARRCOM ATTN: Systems Analysis Office, DRSAR-PE Rock Island, IL 61299	01
Director, Combat Developments US Army Armor Center ATTN: ATZK-CD-MS Fort Knox, KY 40121	02
Commander US Army Test & Evaluation Command ATTN: DRSTE-CT-C Aberdeen Proving Ground, MD 21005	01
Commander Harry Diamond Laboratories ATTN: Library 2800 Powder Mill Road Adelphi, MD 20783	01
Director US Army Ballistic Research Labs ATTN: DRXBR-LB Aberdeen Proving Ground, MD 21005	01

DISTRIBUTION LIST (CONTD)

Address	No. of Copies
Director US Army Human Engineering Labs Aberdeen Proving Ground, MD 21005	01
Director US Material Systems Analysis Activity ATTN: DRXSY-T Aberdeen Proving Ground, MD 21005	01
Director US Army Material Systems Analysis Activity ATTN: DRXSY-MP Aberdeen Proving Ground, MD 21005	01
Chief CECOM Aviation Electronics Office ATTN: DRSEL-MME-LAF(2) St. Louis, MO 63166	01
Commander AVSCOM ATTN: DRSAV-E PO Box 209 St. Louis, MO	01
Commander ARRADCOM ATTN: DRDAR-LIN-S (Bldg 95) Dover, NJ 07801	01
Commander ARRADCOM ATTN: DRDAF-TSS, #59 Dover, NJ 07801	01
Director Joint Communication Office (TRI TAC) ATTN: TT-AD (Tech Doc Cen) Fort Monmouth, NJ 07703	01
PM, FIREFINDER/REMBASS ATTN: DRCPM-FER Fort Monmouth, NJ 07703	01
Commander CECOM ATTN: DELS D-L ATTN: DELS D-L-S(STINFO) Ft. Monmouth, NJ 07703-5301	01 03

DISTRIBUTION LIST (CONTD)

Address	No. of Copies
	01
Project Manager NAVCON ATTN: DRCPM-NC-TM Fort Monmouth, NJ	
	02
Commander US Army Satellite Communications Agency ATTN: DRCPM-SC-3 Fort Monmouth, NJ 07703	
	01
TRI-TAC Office ATTN: TT-SE Fort Monmouth, NJ 07703	
	01
Commander US Army Avionics Lab AVRADA ATTN: SAVAA-D Fort Monmouth, NJ 07703	
	01
Commander US Army Research Office ATTN: Dr. Horst Wittmann PO Box 12211 Research Triangle Park, NC 27709	
	02
Commander US Army Research Office ATTN: DRXRO-IP PO Box 12211 Research Triangle Park, NC 27709	
	02
Commander US Army Research Office ATTN DRXRO-PH (Dr. R. J. Lontz) Research Triangle Park, NC 27709	
	02
Commandant US Army Inst For Military Assistance ATTN: ATSU-CTD-MO Fort Bragg, NC 28307	
	01
Commandant USAFAS ATTN: ATSF-CD-DC Fort Sill, OK 73503	

DISTRIBUTION LIST (CONTD)

Address	No. of Copies
Commandant US Army Air Defense School ATTN: ATSA-CD-MS-C Fort Bliss, TX 79916	01
Commander AMC ATTN: AMCDE 5001 Eisenhower Avenue Alexandria, VA 22333-0001	01
Director US Army Signals Warfare Ctr. Vint Hill Farms Station ATTN: AMSEL-SW-OS Warrenton, VA 22186 -5100	02
Director US Army Signals Warfare Ctr. ATTN: ATTN: AMSEL-SW-AO Vint Hill Farms Station Warrenton, VA 22186 -5100	01
Commandant US Army Engineer School ATTN: ATZA-TDL Fort Belvoir, VA 22060	02
Commander US Army Engineer Topographic Labs ATTN: ETL-TD-EA Fort Belvoir, VA 22060	01
Commander US Army Logistics Center ATTN: ATCL-MC Fort Lee, VA 22801	02
Commander TRADOC ATTN: TDOC-TA Fort Monroe, VA 23651	01
Commander US Army Training & Doctrine Command ATTN: ATCD-TM Fort Monroe, VA 23651	01

DISTRIBUTION LIST (CONTD)

Address	No. of Copies
Commander US Army Garrison Vint Hill Farms Station ATTN: IAVAAF Warrenton, VA 22186	01
Project Manager Control & Analysis Centers Vint Hill Farms Station Warrenton, VA 22186	01
Commander Night Vision & Electro-Optics Lab CECOM ATTN: CELNV-D Fort Belvoir, VA 22060	01
Commander Atmospheric Sciences Lab LABCOM ATTN: SLCAS-SY_S White Sands Missile Range, NM 88002	01
Chief Office Missile Electronic Warfare Electronic Warfare Lab, LABCOM White Sands Missile Range, NM 88002	01
Chief Intel Material Development & Support Office Electronic Warfare Lab, ERADCOM Fort George G. Meade, MD 20755	01
Commander US Army Ballistic Research Lab/ARPADCOM ATTN: DRDAR-TSB-S (ST INFO) Aberdeen Proving Ground, MD 21005	01
Commander LABCOM ATTN: AMSLC-CT 2800 Powder Hill Road Adelphi, MD 20763-1145	02
Commander LABCOM ATTN: 2800 P Adelphi,	01

DISTRIBUTION LIST (CONTD)

Address	No. of Copies
Headquarters Harry Diamond Laboratories ATTN: SLCHD -TD (Dr. W. W. Carter) 2800 Powder Mill Road Adelphi, MD 20783 -1145	01
MIT - Lincoln Laboratory ATTN: Library (RM A-082) PO Box 73 Lexington, MA 02173	01
NASA Scientific & Tech Information Facility Baltimore/Washington Intl Airport PO Box 8757, MD 21240	01
National Bureau of Standards Bldg 225, RM A-331 ATTN: Mr. Leedy Washington, DC 20231	01
Dr. Clayton Paul Electrical Engineering Dept University of Kentucky Lexington, KY 40506	01
Mr. John Spina RADC/RBCT Griffiss AFB, NY 13441	01
Commander US Army Communications Research & Development Command ATTN: DRDCO-SEI-A/Mr. Sam Segner Fort Monmouth, NJ 07703	01
Commander US Army Communications-Electronics Command ATTN: AMSEL -COM-D Fort Monmouth, NJ 07703	01
Commander US Army Communications - Electronics Command ATTN: AMSEL-COM-AY-2/Mr. Stuart Altert Fort Monmouth, NJ 07703 -5202	15